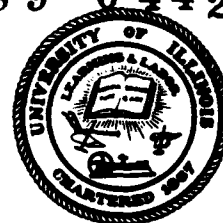


DTIC FILE COPY

AFOSR-TR. 89-0442

2

Department of Mechanical and
Industrial Engineering
University of Illinois at
Urbana-Champaign
Urbana, IL 61801



UIIU ENG-88-4014

SPECTROSCOPIC DIAGNOSTICS OF ELECTRON TEMPERATURE AND ENERGY CONVERSION EFFICIENCY OF LASER-SUSTAINED PLASMA IN FLOWING ARGON

Approved for public release;
distribution unlimited.

J. Mazumder and H. Krier
Co-Principal Investigators

and

X. Chen
Graduate Research Assistant

Annual Technical Report submitted to
Air Force Office of Scientific Research
Dr. Mitat Birkan, Program Manager
for research conducted
during the period
1 September 1987 to 8 August 1988
under
Grant No. AFOSR-87-0169

August 1988

Approved for public release;
distribution unlimited

DTIC
ELECTE

APR 13 1989

H

Approved for public release and is
available to the public through the
Air Force Office of Scientific Research (AFOSR)
Chief, Technical Information Division

AD-A207 054

89

1

12

038

REPORT DOCUMENTATION PAGE

1a. REPORT SECURITY CLASSIFICATION Unclassified		1b. RESTRICTIVE MARKINGS none	
2a. SECURITY CLASSIFICATION AUTHORITY		3. DISTRIBUTION/AVAILABILITY OF REPORT Approved for Public Release; Distribution is Unlimited	
2b. DECLASSIFICATION/DOWNGRADING SCHEDULE			
4. PERFORMING ORGANIZATION REPORT NUMBER(S) UILU-ENG-88-4014		5. MONITORING ORGANIZATION REPORT NUMBER(S) AFOSR-TR-89-0442	
6a. NAME OF PERFORMING ORGANIZATION University of Illinois at Urbana-Champaign	6b. OFFICE SYMBOL (If applicable) NA	7a. NAME OF MONITORING ORGANIZATION AFOSR/NA	
6c. ADDRESS (City, State, and ZIP Code) Dept. of Mech/Ind Engineering 1206 West Green St., Urbana, IL 61801		7b. ADDRESS (City, State, and ZIP Code) Building 410, Bolling AFB, DC 20332-6448	
8a. NAME OF FUNDING/SPONSORING ORGANIZATION AFOSR/NA	8b. OFFICE SYMBOL (If applicable) AFOSR NA	9. PROCUREMENT INSTRUMENT IDENTIFICATION NUMBER AFOSR Grant No. 87-0169 and 88-0129	
8c. ADDRESS (City, State, and ZIP Code) Building 410, Bolling AFB Washington, DC 20332-6448		10. SOURCE OF FUNDING NUMBERS	
		PROGRAM ELEMENT NO. 61102H	PROJECT NO. 2308
		TASK NO. A1	WORK UNIT ACCESSION NO.
11. TITLE (Include Security Classification) Spectroscopic Diagnostics of Electron Temperature and Energy Conversion Efficiency of Laser-Sustained Plasma in Flowing Argon			
12. PERSONAL AUTHOR(S) J. Mazumder, H. Krier, and X. Chen			
13a. TYPE OF REPORT	13b. TIME COVERED FROM 9/1/87 TO 8/8/88	14. DATE OF REPORT (Year, Month, Day) 1988 August 25	15. PAGE COUNT 91
16. SUPPLEMENTARY NOTATION			
17. COSATI CODES		18. SUBJECT TERMS (Continue on reverse if necessary and identify by block number)	
FIELD	GROUP	SUB-GROUP	
		Laser-sustained plasmas, Spectroscopy of plasmas, Beamed energy conversion.	
19. ABSTRACT (Continue on reverse if necessary and identify by block number)			
<p>19. ABSTRACT Laser-sustained plasmas are often formed during laser materials interaction. The University's 10 kW CW CO₂ laser has been used to study argon plasmas for the application to laser-supported propulsion and laser materials processing. The spectroscopic diagnostic method has been applied to study laser-sustained plasmas in 1 atmosphere pure argon gas flow with an f/7 on-axis laser focusing scheme. High flow speeds of 2 to 10 m/sec are achieved. Plasma electron temperature distributions are determined from the 415.8 nm ArI line and its adjacent continuum intensities. Plasma core temperatures as high as 20,000 K are reported. The total absorption of the incident laser power and the radiation loss by the plasma are calculated from the temperature distribution. Results indicated that up to 86 percent of the incident laser power can be absorbed and nearly 60 percent of the incident laser power can be retained by the flowing argon gas to provide thrust.</p> <p>Further research is called for in the laser-induced fluorescence (LIF) technique for diagnostics of the downstream mixing zone and the plasma outer region. Experiments over a wider range of operating conditions, as well as multiple plasma testings, are required to find the optimum operating scheme.</p>			
20. DISTRIBUTION/AVAILABILITY OF ABSTRACT <input checked="" type="checkbox"/> UNCLASSIFIED/UNLIMITED <input checked="" type="checkbox"/> SAME AS RPT. <input checked="" type="checkbox"/> DTIC USERS		21. ABSTRACT SECURITY CLASSIFICATION Unclassified	
22a. NAME OF RESPONSIBLE INDIVIDUAL Dr. Mitat Birkan		22b. TELEPHONE (Include Area Code) 202-767-4938	22c. OFFICE SYMBOL AFOSR/NA

Abstract

Laser-sustained plasmas are often formed during laser materials interaction. The university's 10 kW CW CO₂ laser has been used to study argon plasmas for the application to laser-supported propulsion and laser materials processing. Spectroscopic diagnostic method has been applied to study laser-sustained plasmas in 1 atmosphere pure argon gas flow with an f/7 on-axis laser focusing scheme. High flow speed of 2 m/sec to 10 m/sec are achieved. Plasma electron temperature distributions are determined from the 415.8 nm ArI line and its adjacent continuum intensities. Plasma core temperatures as high as 20,000 K are reported. The total absorption of the incident laser power and the radiation loss by the plasma are calculated from the temperature distribution. The results indicate that up to 86% of the incident laser power can be absorbed and that nearly 60% of the incident laser power can be retained by the flowing argon gas to provide thrust.

Further research is called for in the laser-induced fluorescence (LIF) technique for diagnostics of the downstream mixing zone and the plasma outer region. Experiments over a wider range of operating conditions, as well as multiple plasma testings are required to find the optimum operating scheme.



Accession For	
NTIS GRA&I	<input checked="" type="checkbox"/>
DTIC TAB	<input type="checkbox"/>
Unannounced	<input type="checkbox"/>
Justification	
By _____	
Distribution/	
Availability Codes	
Dist	Avail and/or Special
A-1	

Table of Contents

iv

	Page
Chapter 1: Overview of Laser Sustained Plasmas	1
1.1 Introduction.	1
1.2 Laser-Supported Propulsion	2
1.3 Review of Research on Laser-Sustained Plasmas.	5
1.4 Research Objectives	7
Chapter 2: Theory and Background	9
2.1 Plasma Initiation and Absorption.	9
2.2 Plasma Radiation	12
2.3 Spectroscopic Diagnostics	17
Chapter 3: Experimental Facility.	20
3.1 The Laser and the Laser Lab.	20
3.2 Plasma Test Stand	21
3.3 OMA and Optical Diagnostics	26
3.3.1 Plasma Imaging Optics and Spectrograph	28
3.3.2 Optical Multichannel Analyzer.	32
3.3.3 Translation Stage and Stepping Motor-Controller	33
Chapter 4: Experimental Procedure and Data Analysis	35
4.1 Alignment	35
4.1.1 Alignment of Plasma Imaging Optics.	36
4.1.2 Alignment of Monochromator and Vidicon Detector Head.	40
4.2 OMA Operations	42
4.3 Finding the Plasma	45
4.4 Data Acquisition	47
4.5 Laser Power Measurement and Beam Analysis.	48
4.6 Data Reduction	51
4.6.1 Preliminary Data Reduction on OMA	51
4.6.2 Abel Inversion and Temperature Determination.	56
4.6.3 Absorption and Efficiency Calculation	57
Chapter 5: Results, Discussion and Recommendations	59
5.1 Plasma Temperature Distribution.	59
5.2 Total Absorption and Thermal Efficiency.	64
5.2.1 Total Absorption	68
5.2.2 Thermal Efficiency.	70
5.3 Comparison with Calorimeter-Thermocouple Measurements	72
5.4 Recommendations	76
Appendix A: Program to Drive Stepping Motor Controller.	80
Appendix B: Program to Do 2-D Temperature Contour	81
References	86

Chapter 1: Review of Laser-Sustained Plasmas

1.1 Introduction

Laser technology has been fast growing ever since the invention of the first laser device in the early 1960's. Some of the important industrial applications involve substantially high laser intensity that plasmas will be at present during the interaction of the laser beam with the material. Such applications include laser welding, cutting, alloying and cladding. The plasma is often referred to as the fourth state of a substance consisting of either ions only (fully ionized plasma) or both ions and atoms (partially ionized plasma) from the material and the ambient gas. With the use of high peak power pulsed laser or high power CW laser, energy flux of greater than 10^8 W/cm² can be achieved and the effect of enhanced coupling happens where more laser energy is coupled into the material than that predicted by simple absorption and heat conduction. Apparently the plasma plays a very important role in this effect.

Another area of interest for laser-sustained plasmas is the laser supported rocket propulsion, where a high power laser beam is focused in a flow chamber of propellant gas to form and sustain a plasma. Laser energy is first absorbed by the plasma whose temperature can reach as high as 20,000 K. After the radiation loss, the plasma energy then is coupled into thermal energy of the flowing propellant gas by downstream mixing and the hot gas is further expanded through a nozzle to produce propulsion. It is clearly seen that again the plasma plays the role of energy conversion between the laser and the material. Therefore it becomes essential to have a good understanding of the properties of the laser-sustained plasma (LSP).

Although some experiments were done on the laser-aluminum interaction in the early stages of the research, this report will focus on the LSP's formed in laser-gas interaction and its applications in laser supported propulsion.

1.2 Laser Supported Rocket Propulsion

The existing rocket propulsion systems, namely the chemical or electric propulsion, have nearly approached their limit of potential development (see Figure 1.1). But the demand is still increasing rapidly for transferring payloads from low earth orbits to geosynchronous orbits such as positioning communications satellites. Obviously a more efficient propulsion system must be found with increased payload mass in order to lower the cost.

The idea of laser propulsion was first proposed in 1972 by Kantrowitz [1], that a ground or space-based high power laser be used as a remote energy source, avoiding the undesired heavy load of chemical system or power source in the present propulsion systems. As shown in Figure 1.2, the laser is focused into an absorption chamber in which laser energy is coupled to a flowing propellant gas. The gas will be heated to extremely high temperatures and exhausted out of a conventional rocket nozzle to produce thrust. This system is believed to be able to produce a moderate level of thrust (up to 10 KN) at a relatively high specific impulse (more than 1,000 sec). Additionally the spacecraft is considerably lighter because the laser and its power source are not on board.

It is estimated that a minimum laser power of 10 MW is required to produce a significant thrust of more than 1 KN [2]. Therefore current CO₂ lasers with maximum powers of 10 to 100 KW are not enough for practical use. However a few high power laser systems are currently under investigation which include chemical, free electron and X-ray lasers. Laser powers of 50 to 100 MW are expected to be available within 20 years. Meanwhile CO₂ lasers are chosen to study the interaction of laser with the propellant gas in an effort to understand the process. The key is to maximize the thermal conversion efficiency defined as the rate of thermal energy retained by the

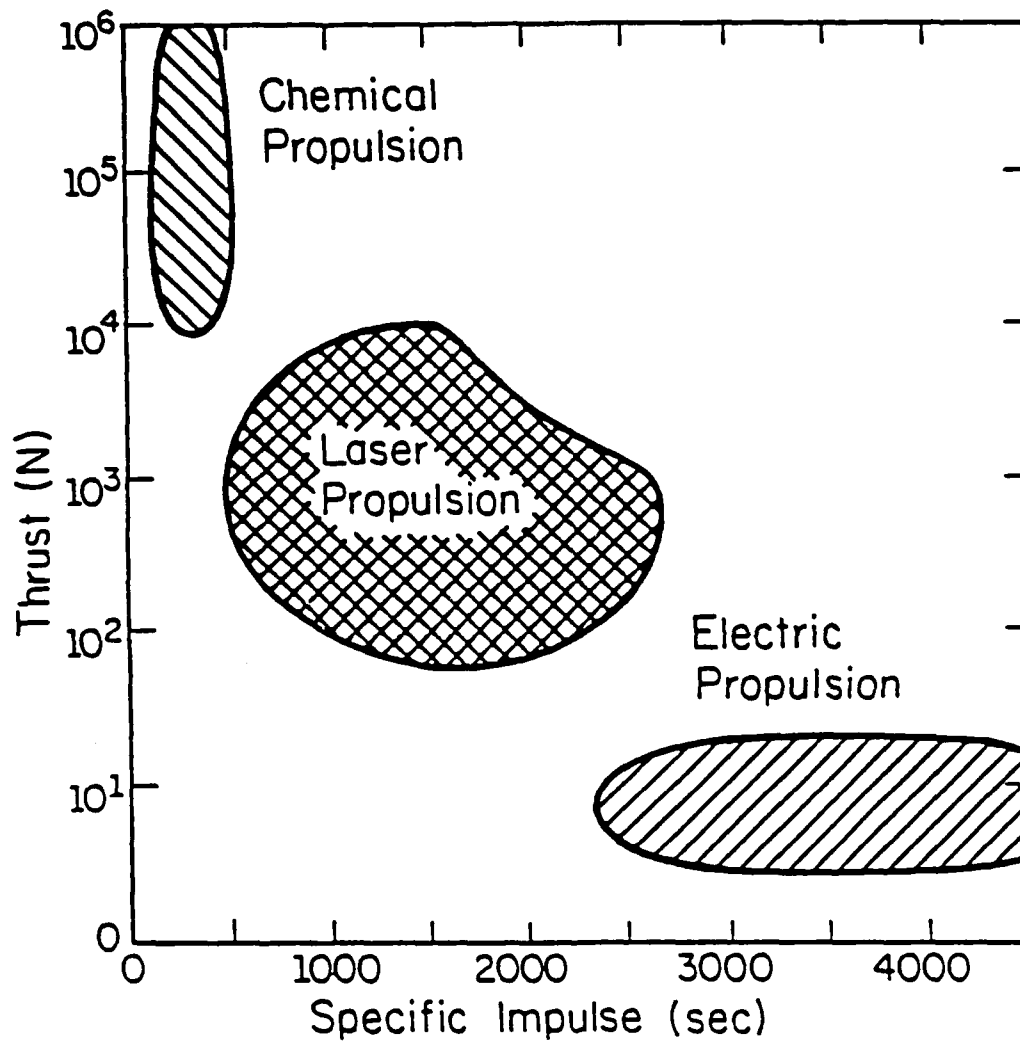


Figure 1.1 Thrust and Specific Impulse (I_{sp}) Comparison. Laser propulsion is expected to fill the gap between the two conventional propulsion systems. [2]

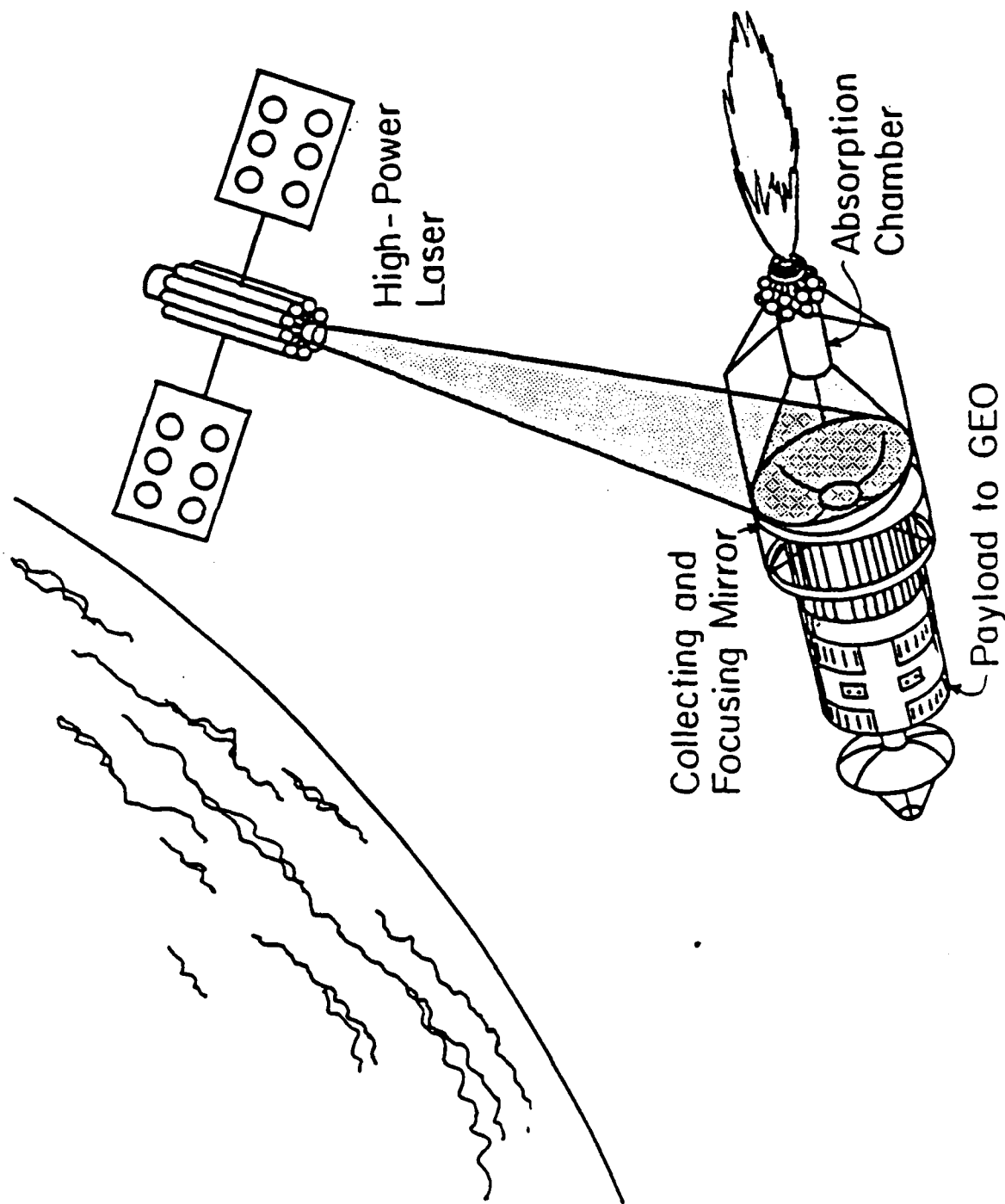


Figure 1.2 Schematic of laser rocket propulsion system at work. [2]

propellant gas exhausted out of the nozzle divided by the incoming laser power.

Several techniques have been proposed for the energy conversion from laser to propellant gas. A good review can be found in reference [3]. Both pulsed and continuous wave (CW) lasers were discussed. Direct laser heating which directly couples the laser energy to the cold propellant, and laser-sustained plasmas have been the two major schemes for energy conversion, each having its own advantages and disadvantages. In this research we will concentrate on CW CO₂ laser-sustained plasmas, which seems to be the most promising energy conversion scheme at this time.

1.3 Review of Research on Laser-Sustained Plasmas

The first experiment of this type was conducted by Fowler and Smith [4] in atmospheric pressure air using a 15 KW CO₂ laser. An interferometric technique was utilized to obtain electron number density in the plasma, and plasma temperature distribution was further calculated, resulting in a peak temperature of 15,000 K. The absorption was found to be about 50% of the laser power and rose with laser power. Plasma radiation was cited as the most important energy loss mechanism. Also found was that a plasma tends to be more stable in a converging beam so long as the f number did not exceed 10.

VanZandt and McCay [5] at NASA Marshall used a 6 joule pulsed and a 30 KW CW CO₂ laser to ignite and maintain LSP respectively, finding that LSP's could be initiated and sustained in pressurized hydrogen flow. The output from a filtered video camera was computer analyzed to get an absolute intensity profile of the continuum radiation of the plasma, from which an electron temperature distribution was calculated.

Keefer [6,7] at the University of Tennessee Space Institute (UTSI) improved VanZandt's diagnostic system and used a 1.5 KW CW CO₂ laser. Argon flew through a

small quartz chamber to create a forced convective environment in the plasma core. A typical plasma was 5 mm in diameter and 10 mm long, with a peak temperature of 16,000 K. Size and position variations on laser power, flow rate and beam geometry were studied within a limited available range of the parameters. It should be noted that the absolute intensity of the continuum emission of the plasma must be calibrated against a calibration source, which requires the local thermodynamic equilibrium. Also the reflection of plasma radiation from the quartz walls could not be eliminated.

Recently Keefer [8] employed a new CO₂ laser which has a Gaussian beam profile. The fractional power absorbed from the Gaussian beam was found to be smaller than that for the annular beam, but the power utilized in heating the flow was larger. A numerical calculation also found that plasmas sustained with shorter wavelength lasers were longer in axial extent, and that they absorbed a smaller fraction of the incident beam power.

Carlhoff [9] also used the absolute continuum method to study high pressure non-flowing argon and helium using a 2 KW CO₂ laser. Minimum maintenance power was found to decrease with pressure until radiation loss became more important. Also the plasma was found to be more stable with higher f number optics.

Krier, Mazumder and the group [10-13] at the University of Illinois at Urbana-Champaign (UIUC) performed the LSP experiments in a pressurized argon flow chamber. The university's 10 KW CW CO₂ laser facility was used. Spectroscopic diagnostic technique was developed using the more accurate line-to-continuum method with the help of the Optical Multichannel Analyzer (OMA) system to map the plasma temperature distribution, showing peak temperatures of nearly 20,000 K. Then the temperature related fractional absorption and radiation were calculated, leading to the obtainment of the thermal efficiency. As an independent measurement, a calorimeter was used to record the transmitted laser power and thermocouples were used to map

the temperature of the downstream gas mixing zone to evaluate absorption and thermal efficiency. The experiments were done over a range of laser power, beam f number, gas flow rate and pressure. Global absorptions of up to 80% and thermal efficiencies of 25% were reported. More recently [14] the thermocouple technique was modified and twin plasma experiments performed in an effort to raise the thermal efficiency. At the same time numerical modelling work [15] have been done. In addition to show a good agreement with the experimental results, it also generates encouraging indications of new operating conditions.

1.4 Research Objectives

The main task of this continuing research is to extend the spectroscopic diagnostics of the laser-sustained plasma to a wider range of operating conditions, such as beam f number, flow rate and pressure. As described earlier, laser energy is first absorbed by the plasma. But not all the absorbed energy will be retained by the flowing gas due to plasma radiation. Therefore it is essential to find the optimum operating condition when the fractional absorption is high while the radiation loss is relatively low, resulting in a high thermal conversion efficiency.

Optical Multichannel Analyzer (OMA) is used with a silicon intensified target (SIT) and a monochromator to acquire the 415.8 nm argon line spectra from an LSP of a flowing argon gas. After an Abel inversion, the ratio of the line intensity to its adjacent continuum intensity is used to calculate the local electron temperature distribution. Temperature contour plots are made to demonstrate the size, length and relative position of the plasma, and this information has been very helpful in explaining some of the plasma characteristics. Since the absorption coefficient can be described as a function of the local electron temperature, fractional absorption is calculated by sending the laser beam through the plasma temperature field pre-

obtained and summing along the beam path. Radiation loss is accounted for by adding up radiation from every point of the plasma due to the fact that radiation intensity is also a function of electron temperature. Thermal energy retained by the flowing gas is then the difference between absorbed and radiated energy. Thermal efficiency is thus calculated.

The 10 KW CW CO₂ laser can operate steadily at a maximum power of 9 KW. And by the time the laser beam reaches the gas flow chamber it is only 7 KW due to loss on the optics. Different focal length lenses are used to form beam f numbers of f/4 to f/7. Gas flow chamber pressure can be varied from 1 to 2.5 atmospheric pressure.

Various aspects of this investigation are presented in the following chapters. Chapter 2 addresses the background physics of the LSP and the theoretical basis of the spectroscopic diagnostic method. Chapter 3 is a description of the experimental apparatus and arrangement, while the experimental procedure and data reduction can be found in chapter 4. And lastly the important results, discussions and recommendations for future work are included in chapter 5.

Chapter 2: Theory and Background

As pointed out in Chapter 1, laser-sustained plasmas (LSP's) play the key role of converting laser energy into gas thermal energy in laser propulsion. Hence in this chapter, we are going to explore the physics behind the various processes during the energy conversion, the most important being the power absorption and plasma radiation. Also outlined is the theoretical foundation for our spectroscopic diagnostic technique.

2.1 Plasma Initiation and Absorption

A plasma is a collection of free electrons, ions and neutral atoms. Obviously it must be initiated through ionization processes which break down the originally neutral atoms. Such a process strips an electron off an atom, leaving as a result a pair of positive ion and free electron. The electron number density is equal to the positive ion density so that the plasma is globally electrically neutral.

Two major processes can lead to a plasma initiation in the presence of a laser beam. The first is the multi-photon ionization. A bound electron in an atom absorbs more than one photons simultaneously, gaining enough energy to overcome the ionization potential. For the case of argon, the ionization potential of 15.8 eV is an equivalent of 128 photons of 10.6 micron (CO_2 laser wavelength). Therefore the probability of this process is usually very low unless there is an extremely high laser intensity (10^9 - 10^{12} W/cm²), such as in a pulsed laser beam. In our CW CO_2 laser, however, the intensity is only 10^5 - 10^6 W/cm². Thus we conclude that multi-photon ionization is highly improbable in this investigation.

The other plasma initiation process is through the inverse bremsstrahlung (IB) absorption, but it requires pre-existing free electrons. A laser photon is absorbed by a

free electron in the vicinity of a heavy ion or atom. The electron then transfers its energy through a collision with the nearby heavy particle. If the laser intensity is high enough, the free electron could gain adequate energy to ionize the atom with which it collides. The result is the production of more free electrons available for more IB absorption and ionization processes, causing a cascade or avalanche breakdown.

Because the cold (room temperature) argon gas does not possess any free electrons (or at least not enough), external sources of electron must be provided for the IB process to begin. In this investigation, tungsten rod target is used at the laser focus. Thermionic emission and target vaporization create the initial free electrons and the cascade breakdown leads to the formation of the plasma. The target then is pulled out of the laser path and the plasma maintained by the laser beam. It should be pointed out that inverse bremsstrahlung absorption is responsible for not only the creation but also the maintenance of the plasma.

Figure 2.1 is a schematic of the major physical processes in a laser-sustained flowing gas plasma. The inverse bremsstrahlung absorption coefficient demonstrated in the figure is the result of a classical theory developed by Kramers [16] in 1923 for the electron-ion situation. Later Wheeler [17] and Stallcop [18] made some important corrections to come up with the following semi-classical expression of the inverse bremsstrahlung absorption coefficient:

$$\alpha(\text{m}^{-1}) = \frac{4}{3} \frac{2\pi e^6 Z}{\sqrt{6\pi k m_e^3} hc^4} \frac{N_e^2 \lambda^3}{T_e^{1/2}} \left[1 - \exp(-h\nu/kT_e) \right] \left(g_{ff} + \frac{h\nu}{kT_e} \right) \quad (2.1)$$

where T_e and N_e are the electron temperature and number density respectively, Z the effective ion charge and g_{ff} the free-free Gaunt factor.

Note that in equation (2.1), the coefficient is expressed as a function of N_e and

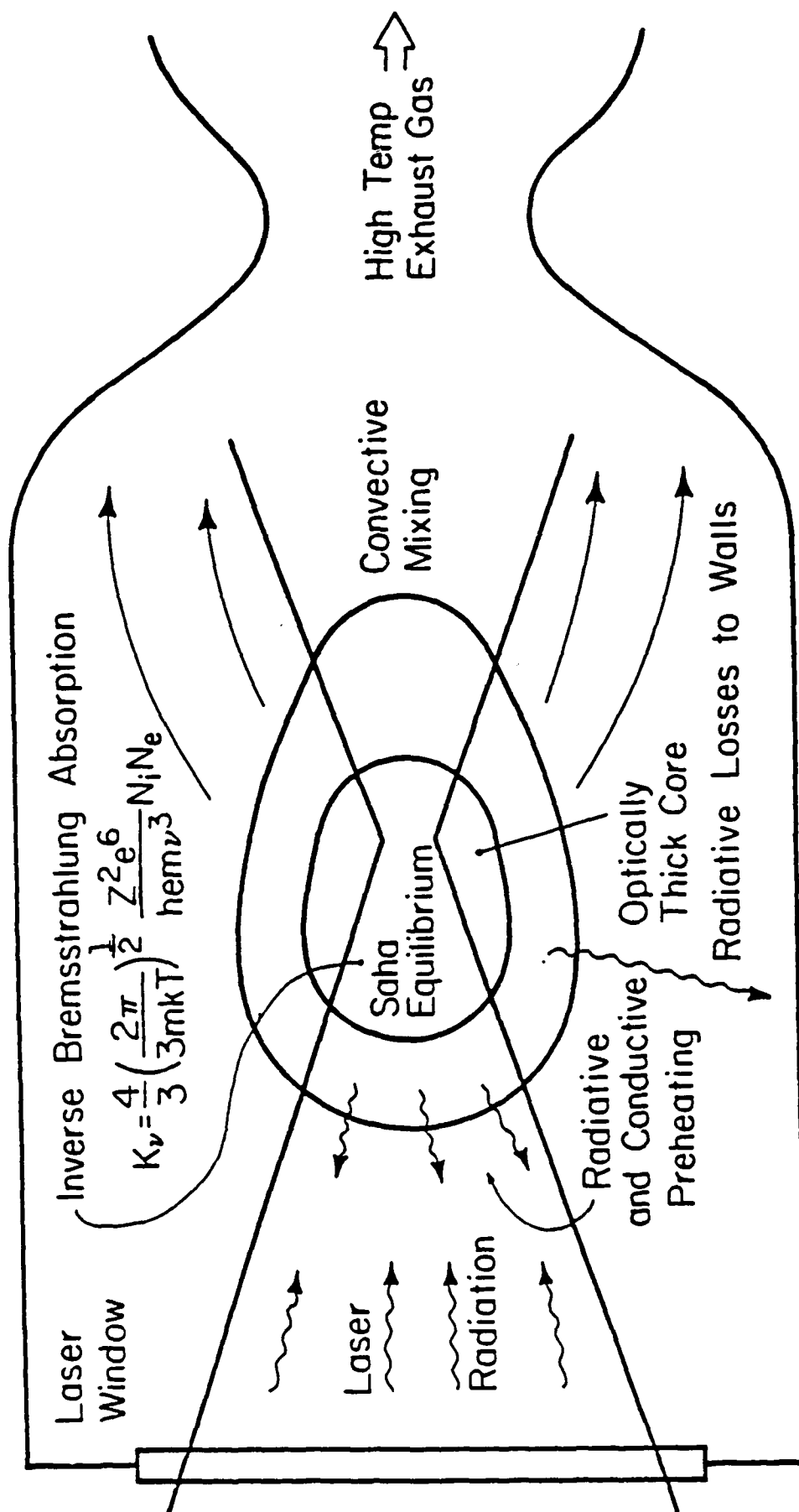


Figure 2.1 Physics of laser-sustained plasma in a gas flow chamber. [2]

T_e . However by using the work in reference [19], N_e becomes a function of T_e . Hence the IB absorption coefficient can be calculated as soon as the electron temperature is obtained. Figure 2.2 and 2.3 show the dependence of electron number density and the IB absorption coefficient on the electron temperature.

The above IB absorption coefficient is valid for cases where local thermodynamic equilibrium (LTE) exists. A simple criteria for determining LTE is that, if the oscillating velocity of an electron in the electromagnetic field of the laser is much smaller than the thermal velocity of the electron, then LTE will be preserved. For our application, temperatures are usually no higher than 20,000K where electron oscillating velocity is at least an order of magnitude smaller than its thermal velocity [20]. Hence the above coefficient is applicable.

Now that the absorption is described as long as the local temperature is specified, we can determine totally how much laser power is absorbed by sending the laser beam through the plasma temperature field and sum the amount along the path. Dividing by the incident laser power yields the total absorption fraction.

2.2 Plasma Radiation

As the primary energy loss mechanism in LSP's, plasma radiation consists of line and continuum emissions. Line radiation comes from photon emission during an electronic transition within the bound states of the atom. And its intensity can be expressed in terms of spontaneous emission:

$$I_{\lambda} = \frac{hcA_{mn}g_m N}{4\pi\lambda Z_e} \exp(-E_m/kT_e) \quad (2.2)$$

However to get the total amount of line radiation we need to account for all the possible electronic transitions, which is a very difficult process. We will discuss this

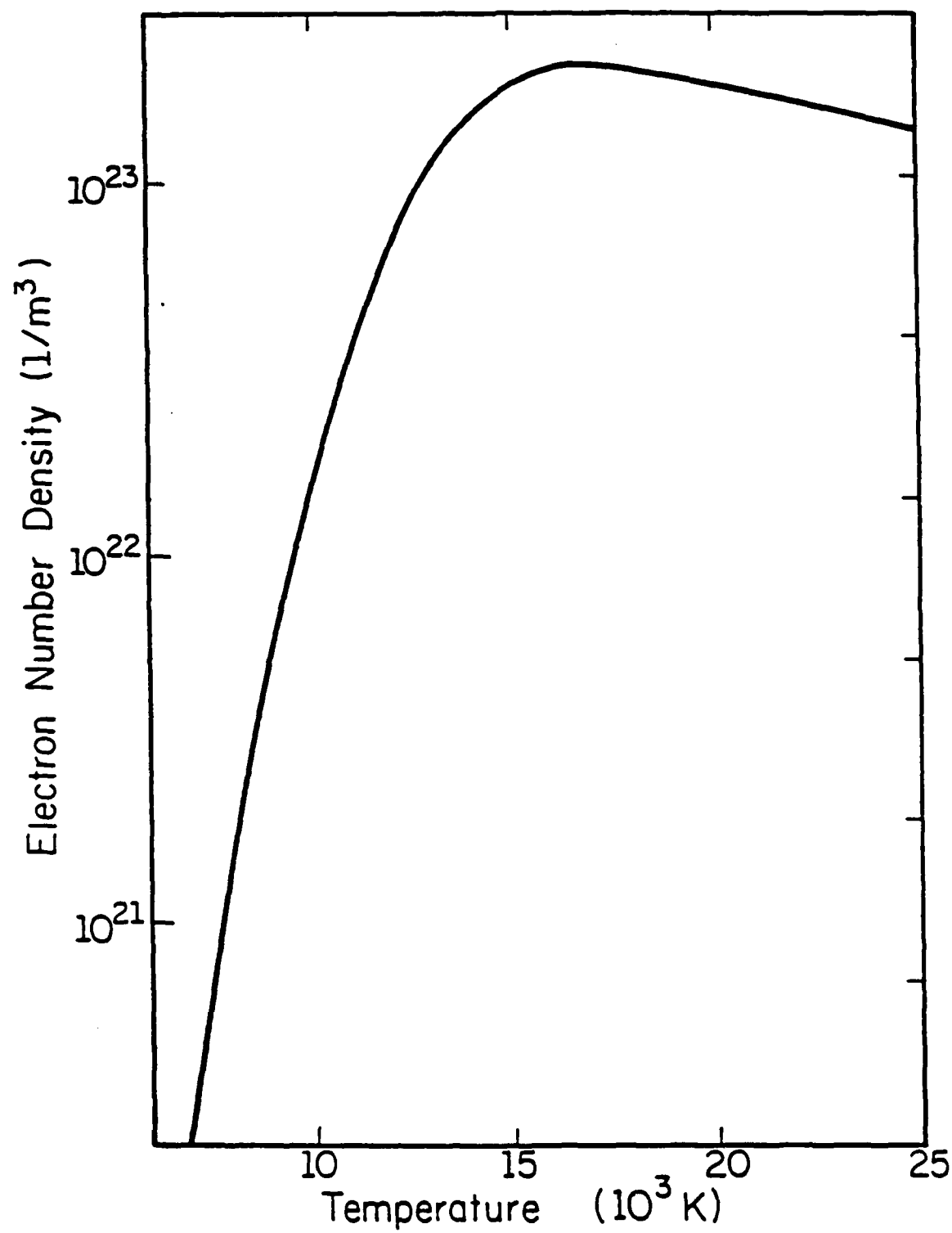


Figure 2.2 Electron number density as a function of electron temperature for 1.0 atm argon. [20]

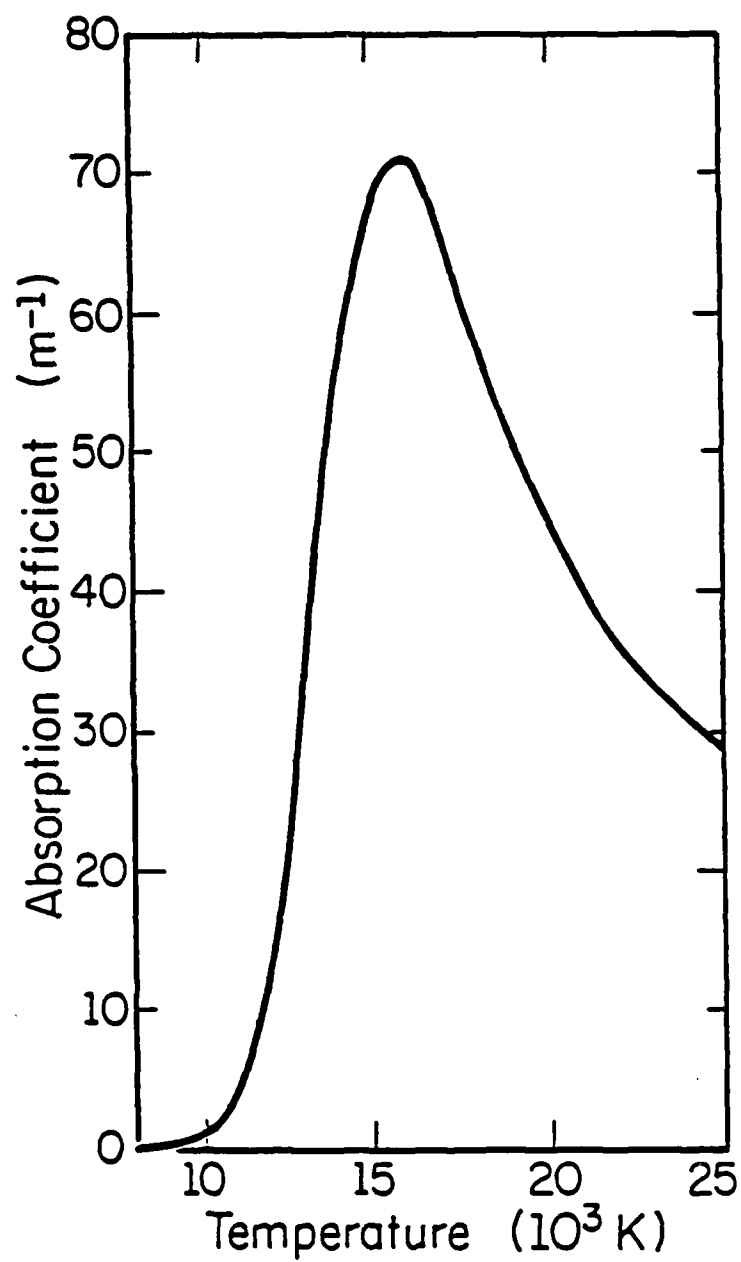


Figure 2.3 Inverse Bremsstrahlung absorption coefficient as a function of electron temperature for 1.0 atm argon. [20]

problem later in this section. But first let us take a look at the continuum part of the plasma radiation.

The continuum radiation in the temperature range encountered is believed to be dominated by the bremsstrahlung radiation. In this process an electron collides with a heavy particle, either an atom or ion, resulting in a slow electron and a particle, with the "lost" kinetic energy being carried away by an emitted photon. By applying the Kramers-Unsold theory, the continuum intensity is described as [19]:

$$I_{c\lambda} = 5.44 \times 10^{-46} \frac{N_e N_i}{T_e^{1/2}} \left[\exp(hc\Delta\lambda/\lambda^2 kT_e) + \exp(-hc/\lambda kT_e)(\bar{g}-1) \right] \zeta(\lambda) \quad (2.3)$$

in which g is the Gaunt factor averaged over the continuum wavelength interval, and the last term is a known function which accounts for the non-hydrogenic behavior of argon.

We mentioned that the line radiation is very difficult to model. Horn [21] went to detail and calculated contributions from numerous lines. Kozlov [22] considered the total radiation as continuum plus contributions from a "smeared" line spectrum. Thus the line radiation is some number times the continuum radiation at a certain temperature. This is presented in Figure 2.4 where both the line and continuum radiation losses are plotted as a function of temperature.

The total radiation loss from the entire plasma volume is then calculated by integrating over all the volume elements. And the system thermal efficiency is defined as:

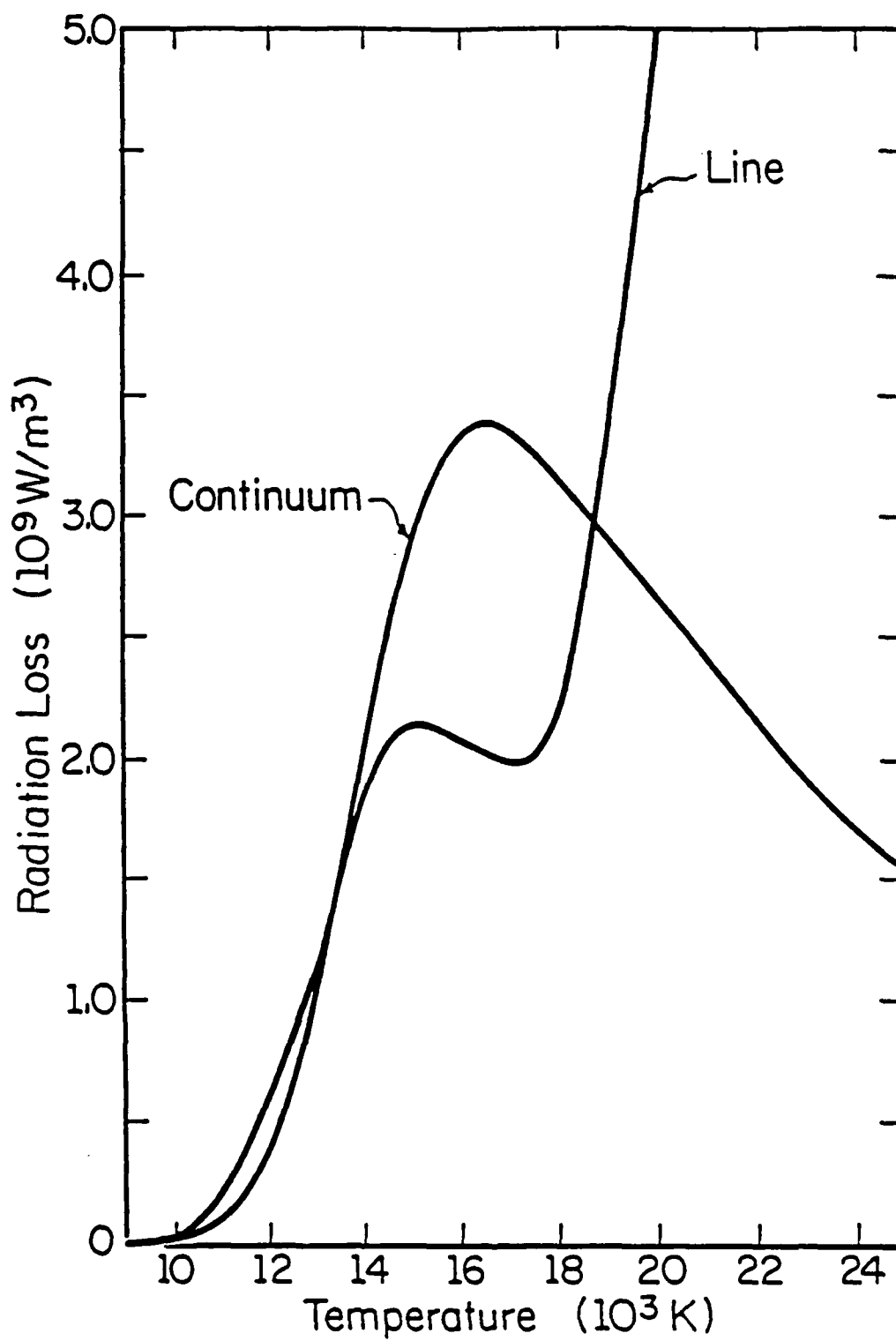


Figure 2.4 Line and continuum radiation as functions of electron temperature for argon. [20]

$$\eta_{th} = \frac{P_{\text{absorbed}} - P_{\text{radiated}}}{P_{\text{incident laser}}} \quad (2.4)$$

where P represents the power.

In this and the previous sections, we found that both total absorption and thermal efficiency can be easily obtained once the plasma temperature distribution is determined. This leads to the next section in which the theoretical basis for the spectroscopic determination of plasma temperature is presented.

Note that when we talk about plasma temperature we mean the electron temperature, because electrons dominate the physical processes encountered in this investigation.

2.3 Spectroscopic Diagnostics

Several spectroscopic techniques have been developed to measure plasma temperature. The most widely used in the study of LSP's are the absolute or relative emission intensity analysis. The absolute techniques [6] make use of a narrow band in the continuum part of the spectrum. The absolute emissive power is measured and compared to a calibrated source to determine the electron temperature. The difficulties in these techniques come from the source calibration and the filter transmission assessment.

The relative line-to-continuum method is used in this investigation. The intensities of a particular spectral line and its adjacent continuum from the same location in plasma are measured, and the ratio is directly related to the local electron temperature. This technique has the advantage of concerning only the relative intensities.

A simplified version of equation (2.2) is employed together with equation (2.3) to get the intensity ratio [20]:

$$I_{\lambda}/I_c = 1.3357 \times 10^{20} (NT_e^{1/2}/N_e^2) \Delta\lambda \quad (2.5)$$

where N is the atom number density, N_e and T_e are the electron number density and temperature, and the continuum band is chosen as 10 angstroms. Since N and N_e are functions of T_e only (see figure 2.2), the above equation states that the line-to-continuum ratio is a one-on-one function of electron temperature, which is illustrated in Figure 2.5. Thus knowing the intensity ratio means getting the local electron temperature.

A signal collected by our detector consists of emissions coming out of all points along the line-of-sight from the detector to the region of interest in the plasma. In other words it is an integrated quantity. To get the local emissive power, the inverse process must be performed which is the Abel inversion. Under the assumption that the plasma is cylindrically symmetric, the local emissive power is expressed in terms of the integrated intensity $I(y)$ as:

$$\epsilon(r) = \frac{1}{\pi} \int_r^{\infty} \frac{dI(y)}{dy} (y^2 - r^2)^{-1/2} dy \quad (2.6)$$

The details of experimental apparatus, data acquisition and reduction techniques are featured in the next chapter.

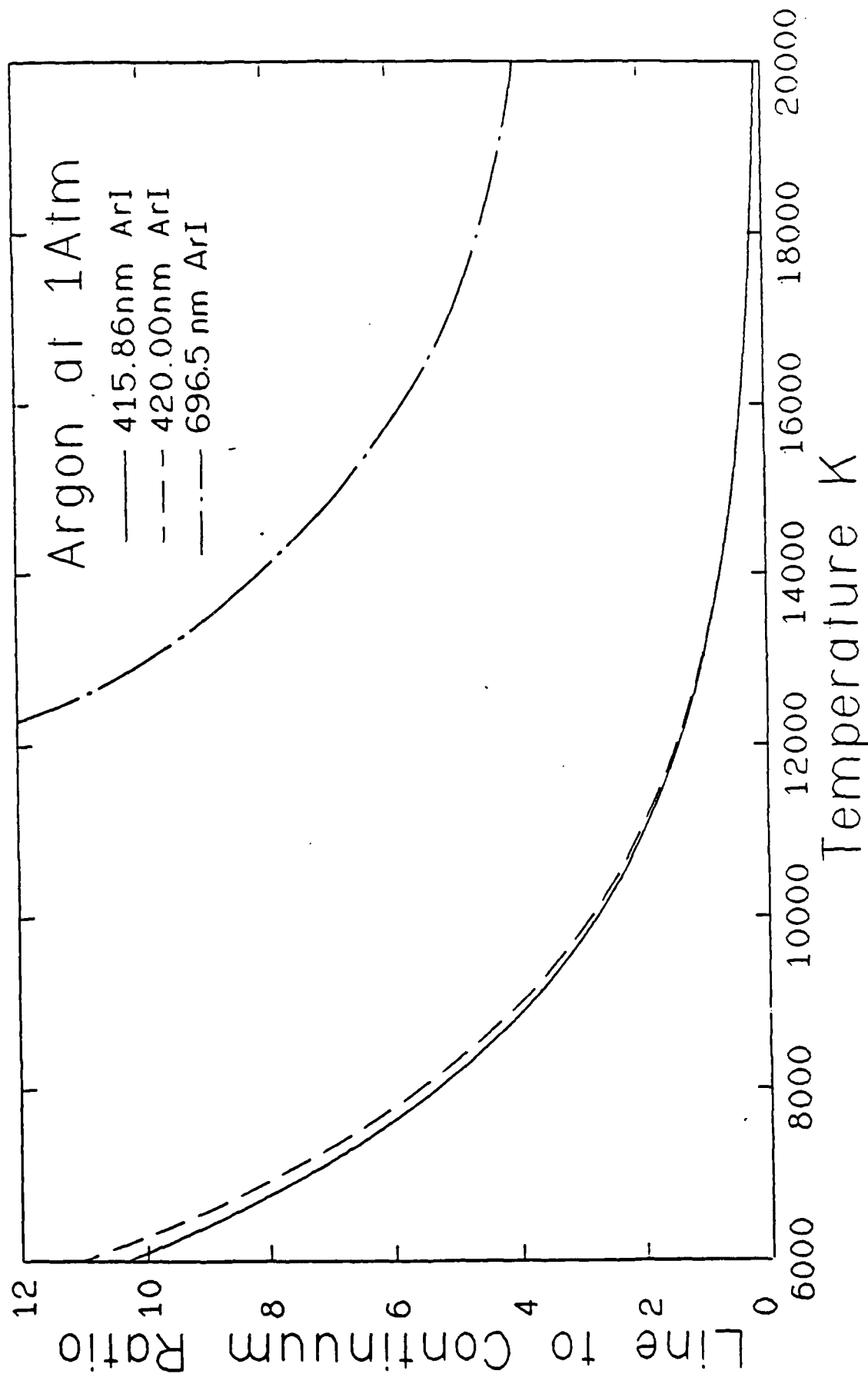


Figure 2.5 Line-to-continuum intensity ratio as a function of electron temperature.
This function is used to determine plasma electron temperature. [20]

Chapter 3: Experimental Facility

The facility used in this investigation can be divided into three major parts: first the 10 KW high power CO₂ laser, then the plasma test stand including the beam focusing optics, the pressurized gas flow chamber and the independent calorimeter-thermocouple equipment, and finally the spectroscopic diagnostic system. Many of the details were described in the early publications of this ongoing research project [2,14,20]. While the main frame of the experimental setup is similar, quite a few changes have been made especially to the laser focusing scheme and the gas flow chamber [23]. This allows the experiments to be run over a wider range of beam f number, gas flow rate and chamber pressure. Also a neutral density filter controller was added to the spectroscopic diagnostic system which makes the filter change faster to speed up the data acquisition process. This chapter is dedicated to highlight the design and functions of the three main sections of the experimental setup.

3.1 The Laser and the Laser Lab

The experiments were done in the Material Engineering Research Lab (MERL) Laser Room located in the Talbot Laboratory. The laser source is a 10 KW continuous wave (CW) Avco Everett HPL-10 CO₂ laser system. It works at variable powers, with a maximum of 9 KW at steady operation over a long period of time required in this investigation (> 1 minute). The laser is an unstable resonator whose output beam has an annular shape similar to a TEM₀₁* mode profile and a wavelength of 10.6 μ m. The inside and outside diameter at the test stand are 46.6 mm and 74.8 mm respectively. The intensity distribution across the annulus is near Gaussian. Beam quality can be greatly improved by readjusting the internal laser optics, but it takes two weeks to perform. However such an adjustment is quite necessary if a severe nonuniform

intensity distribution is detected in the output laser beam.

The laser laboratory arrangement is shown schematically in Figure 3.1. The experimental control room was constructed around the test stand with large safety windows to separate the diagnostic equipment and the experimenter from the laser room. The test stand is located about 8 m away from the laser output window, so that other experiments can be done without interference. This, of course, results in some beam divergence when it reaches the test stand. A laser technician operates the laser from the laser control room and communicates with the experimenter over a headphone. There is also an outside storage area for gas bottles used for the experiment. All the doors to the laser room have safety locks which will automatically shut down the laser upon accidental entry.

3.2 Plasma Test Stand

This part of the experimental setup includes the optics used to bring and focus the laser beam into the chamber, the pressurized gas flow chamber itself and the calorimeter-thermocouple attached to the chamber. The above equipments are mounted on a test stand made of heavy steel unistrut framing, as shown in Figure 3.2. For complete details of the design of the test stand and chamber assembly, please refer to references [2] and [14]. During the course of this investigation, several significant changes were made to the focusing optics and the flow chamber [23]. The important features of the test stand are presented in the following paragraphs.

The output laser beam travels horizontally to reach the first of three turning mirrors and is reflected 90 degrees downward. The second and third mirrors are movable on an optical bench, and are tilted 45 degrees so that the beam is turned twice to enter the gas chamber from below. All three turning mirrors are water-cooled copper flats good for the high power infrared CO₂ laser. High precision

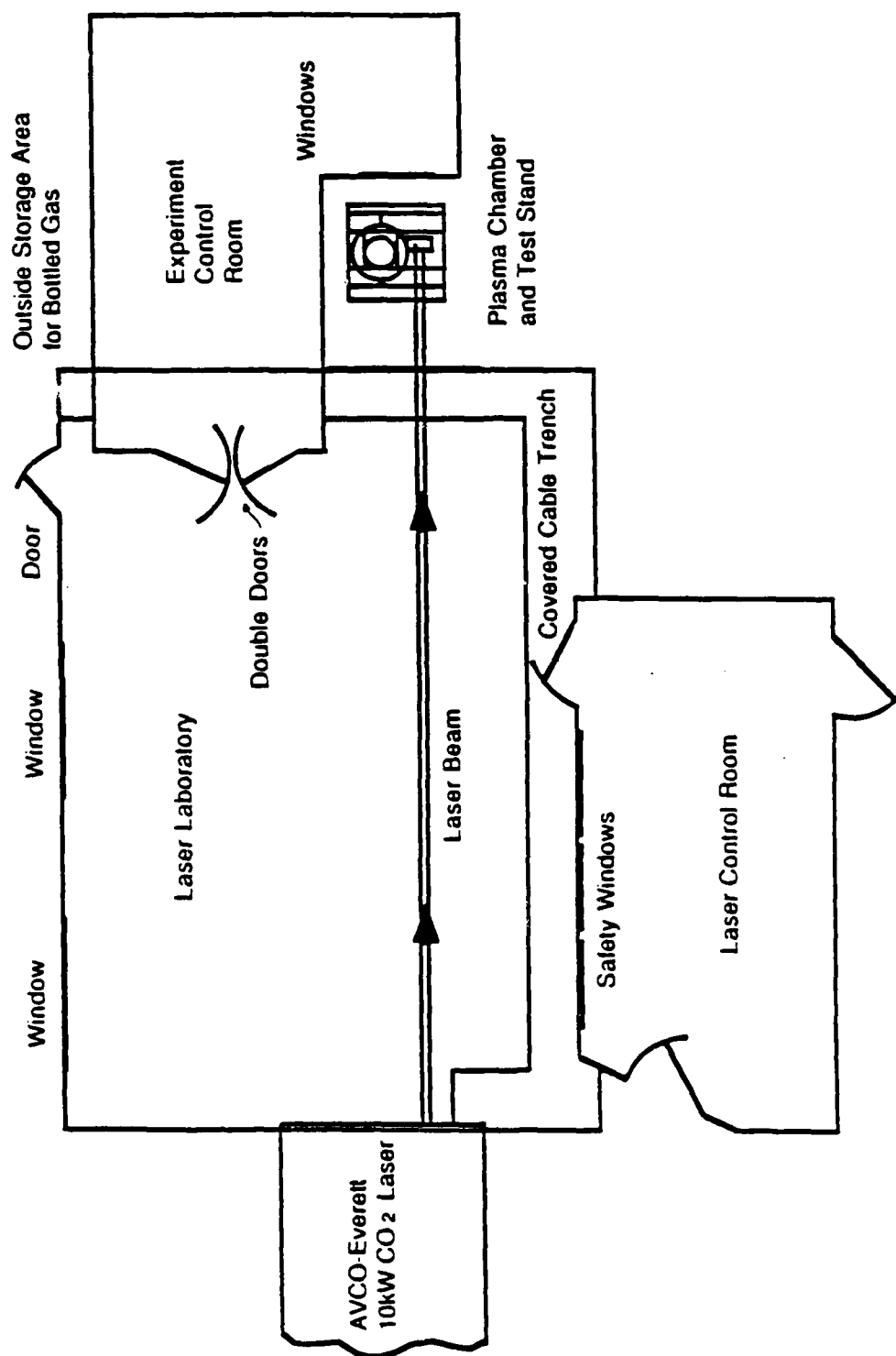


Figure 3.1 Laser laboratory schematic showing the experimental arrangement. [14]

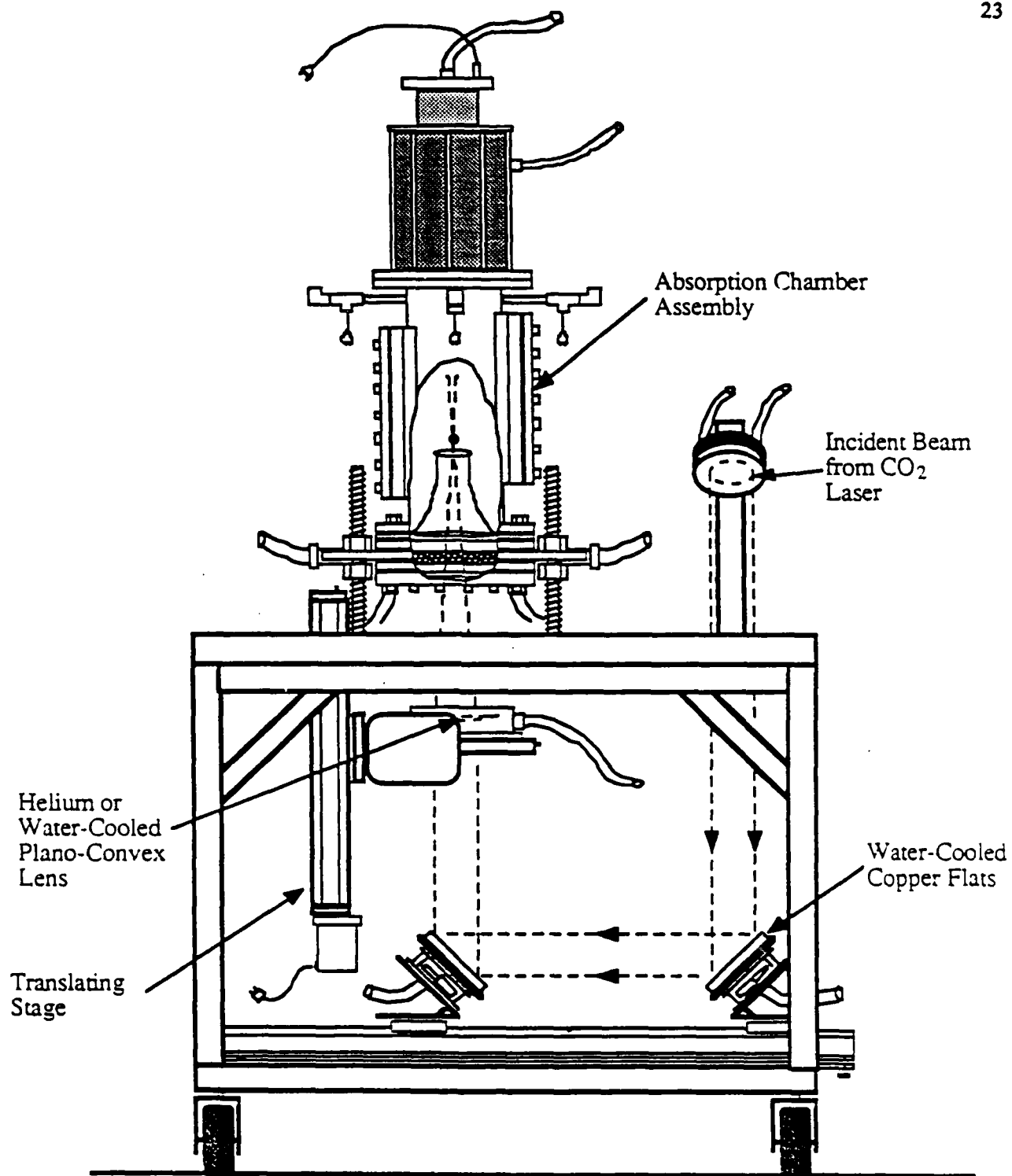


Figure 3.2 Details of the test stand showing the CO₂ laser focusing optics and the absorption chamber assembly. [23]

adjustments on the position and angle of the lower mirrors allow easy fine tuning of the incident beam focus. In the early stages of this investigation, an off-axis convex-concave copper mirror pair was used [14] which allowed f numbers to vary from $f/2$ to $f/3.4$. In the present setup, an on-axis optics is employed using a sodium chloride and later a zinc selenide plano-convex lens. This allows easy change of focusing f numbers by simply selecting lenses of different focal length. The laser beam passes through a sodium chloride or zinc selenide flat window and is focused at a point inside the flow chamber.

Sodium chloride was first selected as the lens and window material because of its high transmittance (more than 95%) at the $10.6\text{ }\mu\text{m}$ CO_2 laser wavelength and its relatively low price. But it has very poor mechanical strength and absorbs moisture to become even more fragile. The ultraviolet radiation from the plasma also darkens the sodium chloride window due to the formation of color centers in the crystal, which is a kind of defect that reduces its strength. In fact the window usually cracks after less than ten 5 minute experimental runs, depending on the original window and polishing quality. Therefore the condition of the window was a big concern during experiments. The sodium chloride lens is relatively long-lived because it is separated from the plasma initiation and flow activities. All sodium chloride parts must be kept clean and dry in a heated oven when not in use.

Zinc selenide, on the other hand, is a much more durable but expensive material. A zinc selenide window costs about 20 times more than a sodium chloride window and a lens more than twice. Also it has a higher index of refraction ($n = 2.403$ compared to 1.491 for sodium chloride), which reduces optical transmittance. But this can be solved by adding an anti-reflective coating to reach more than 99.7% transmission at $10.6\text{ }\mu\text{m}$. Also it has three times higher thermal conductivity than sodium chloride which helps reduce thermal stress built up due to laser heating effect. In addition it

has much better mechanical strength and is moistureproof. Therefore water cooling was employed as opposed to helium gas cooling for sodium chloride parts. The manufacturer suggested safe power density is 1 KW/cm^2 , but tests of more than 1.6 KW/cm^2 were done without failure. Most experimental results presented here were obtained using a zinc selenide window and a sodium chloride lens. In fact the same zinc selenide window has been in use for more than three months. Most recently [24] even the use of sodium chloride lens was abandoned to give way to a zinc selenide lens, completely eliminating sodium chloride parts from the system.

The lens holder is mounted on a translation stage driven by a stepping motor through a Fluke computer in the experiment control room. This permits vertical movement of the plasma after initiation. Since the tungsten target is at a fixed position inside the chamber, this feature enables the repositioning of plasma down into the quartz tube which is added to study the effect of increased flow speed.

The 5 inch inside diameter gas flow chamber was fabricated from stainless steel with two side windows covered by pyrex plates for optical diagnostics. Gas inlet section is located at the lower end of the chamber, so that both the laser beam and the gas flow are directed from bottom to top to minimize the effect of buoyancy. In addition to the 24 randomly oriented gas inlet holes, a sintered stainless steel flow straightener was used to reduce the turbulence in the flow which was responsible for the plasma unstable character at high flow speeds ($> 1 \text{ m/s}$) without a flow straightener. A quartz nozzle made from a tube was added to elevate the flow speed (cm/s) or mass flux ($\text{kg/cm}^2\text{s}$) without increasing the mass flow rate (kg/s). From continuity the increase in speed is proportional to the decrease in cross sectional area. The converging quartz nozzle has an inside diameter of 49 mm at the throat and stable plasmas were sustained at flow speeds of higher than 10 m/s .

At the upper end of the gas flow chamber are four exit ports for the exhaustion

of hot gas. A thermocouple is inserted in each gas inlet and exit port, and the gas temperatures into and out of the chamber are automatically recorded by the Fluke computer. With the knowledge of the mass flow rate, the increase in gas enthalpy is calculated which is used to determine the thermal conversion efficiency. To monitor the chamber wall temperature a thermocouple is embedded in the chamber wall. The reading helps determine how long the plasma experiment can be kept running without overheating the chamber.

A calorimeter is mounted on top of the gas flow chamber. It is a copper cone cooled with water flowing around. All the transmitted laser energy entering the calorimeter will be reflected within the copper cone until completely absorbed. In a steady state condition, this transmitted energy can be measured through thermocouples recording the temperature change in the cooling water. Therefore the calorimeter serves not only as a beam dump but also as an indirect measure of the fraction of incident laser power that is absorbed by the plasma.

The thermocouple-calorimeter system is an independent experimental effort to study the total absorption and thermal efficiency character of the laser-sustained plasmas. Fellow graduate students Dave Zerkle, Ahyan Mertogul and Scott Schwartz are currently involved in this aspect of the project. The recent experimental results were published in reference [24]. Comparisons with the spectroscopic diagnostic results will be made in Chapter 5.

3.3 OMA and Optical Diagnostics

The Optical Multichannel Analyzer (OMA) III system made by EG&G Princeton Applied Research (PARC) was utilized for the optical diagnostics of laser-sustained plasmas. Figure 3.3 is a schematic of the experimental setup. The entire detection system is located in the experiment control room shown in Figure 3.1. Optical access

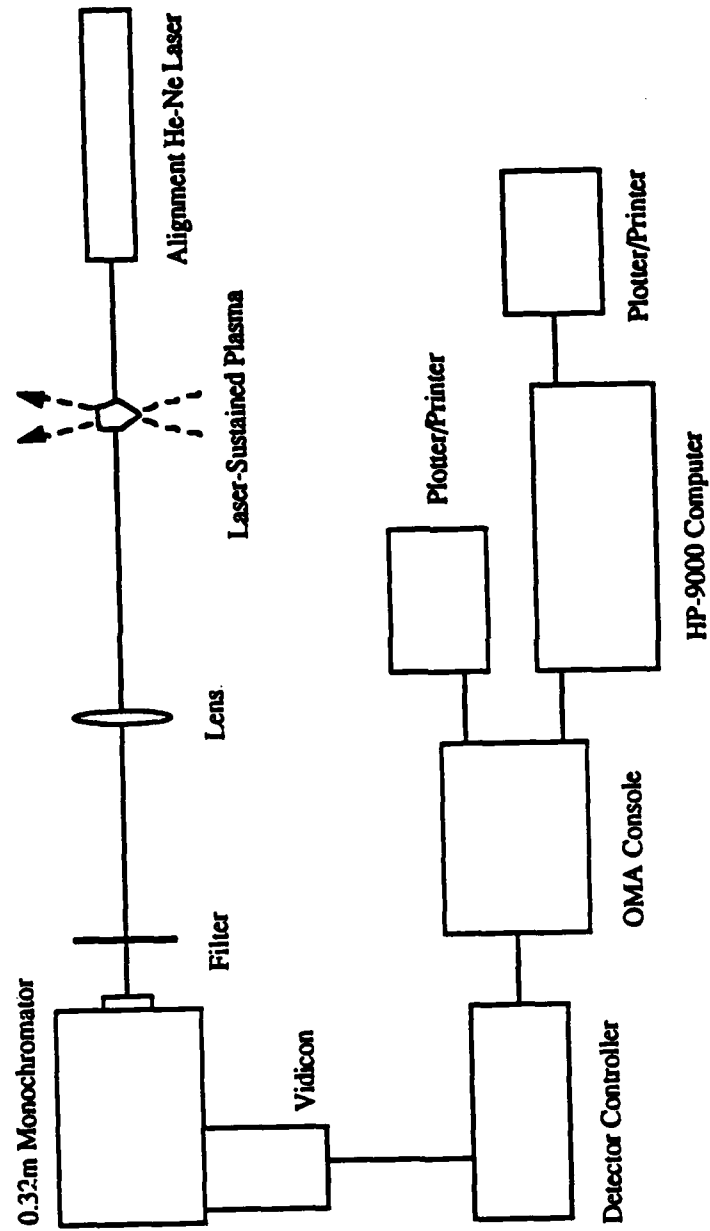


Figure 3.3 Schematic of the experimental setup including the OMA data acquisition and computer systems.

was made possible through the pyrex side window of the gas flow chamber and the large plexiglass window of the experiment control room. The windows are very transparent to visible radiation which is the spectral range of interest. The system can be divided into three sections: first the plasma imaging optics and the spectrograph, then the optical multichannel analyzer system, and third the translation stages and stepping motor-controller assembly.

3.3.1 Plasma Imaging Optics and Spectrograph

An ORIEL plano-convex lens was used to image the plasma onto the monochromator entrance slit (see Figure 3.4). The lens is 3 inches in diameter with a focal length of 20 cm. It is positioned in an ORIEL adjustable diameter optic holder which is mounted on an ORIEL precision rod translator. This assembly provides vertical, horizontal and rotational adjustments of the lens. The translator can be moved along the optical rail to achieve sharp imaging. Also the imaging f number has to match the monochromator f number [25], which is calculated to be $f/4.96$ at the 415.8 nm wavelength. During the alignment process, it is important to make sure that the plasma and the monochromator slit are along the optical axis of the lens. This is done by the use of a HeNe laser beam and will be detailed in the experimental procedures in the next chapter.

The plasma image entering the slit is expanded spectrally by a 0.32 meter coma corrected Czerny-Turner configuration HR-320 spectrograph/monochromator made by Instruments SA, Inc.. It is a rugged, compact instrument which is specifically designed to be operated either as a spectrograph when used with a vidicon or any solid state detector, or as a scanning monochromator when used with a photomultiplier tube (PMT) detector. In this investigation it is used as a spectrograph, although from time to time it might be called a monochromator only because monochromator seems to be

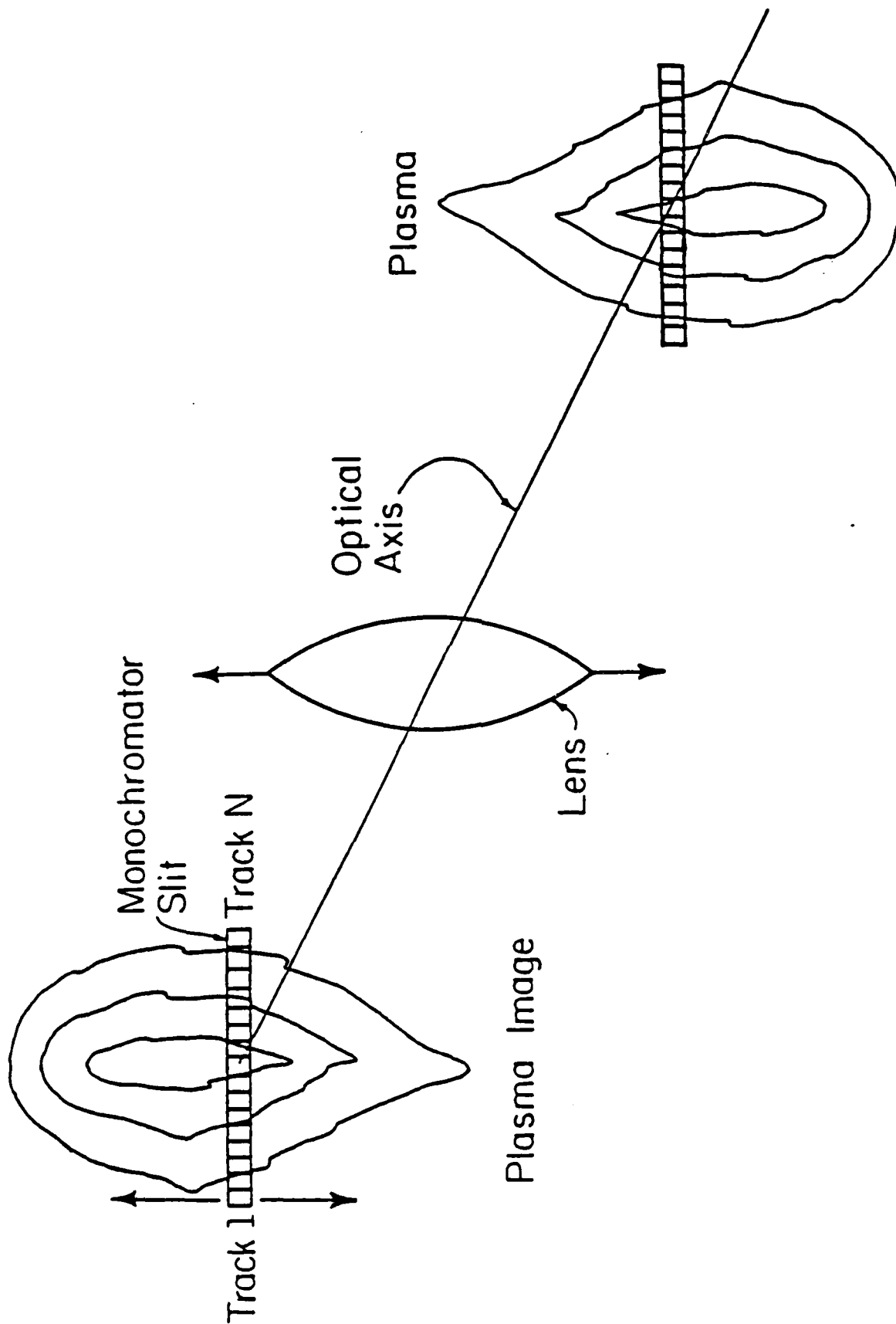


Figure 3.4 Plasma imaging optics. [20]

a more popular name. Three 58x58 mm holographic gratings are available with groove densities of 147 g/mm, 1200 g/mm and 3600 g/mm for different dispersion needs. In the normal data acquisition, 1200 g/mm was used which has a dispersion of 25 angstrom/mm, corresponding to a spectral coverage of about 250 angstroms at the exit port, with a resolution of 0.6 angstroms near the 415.8 nm ArI line.

The smaller groove density grating has larger spectral coverage, thus can be used to observe the entire plasma radiation spectrum. The 3600 g/mm grating, on the other hand, can be used to look into fine structures within the spectrum, since it has greater dispersion. These gratings are easily interchangeable as they are kinematically mounted in the instrument. All the gratings were realigned in their mounts so that it is ready for use upon installation. Special care should be taken, however, in moving the monochromator. A special screw must be tightened on the base of the grating mount in order to keep the alignment.

In December 1987, the monochromator was sent to the manufacturer for realignment, because it started to show alignment problems. An easy indication is that the spectral lines tend to be too wide than they used to be. One can also use standard spectral lamps. Another method is to send a HeNe beam along the optical axis into the monochromator. If the monochromator is perfectly aligned, the beam should come out through the center of the exit port.

Wavelength is selected by turning the wavelength dial. The HR-320 is calibrated and reads direct for a 1200 g/mm grating. For other gratings, the conversion is that the wavelength is indirectly proportional to the groove density. The instructions manual provides a list of the conversion factors.

Fixed slits were used at the monochromator entrance port. The fixed slit assembly consists of a slit housing which fits into a slit support bracket. Fixed slit inserts slide into a slot in the slit housing. The slit used in this experiment is 8 mm

long and 0.025 mm wide, although other slit widths are available at 0.05 mm and 0.1 mm. This is due to the fact that the plasma emission is very strong, allowing the use of narrow slit to take advantage of the better resolution. In fact neutral density filters have to be used in front of the entrance slit to cut down the light intensity to a safe level to the vidicon detector. A narrow slit will also help in this regard.

Because the silicon intensified target is designed as a highly sensitive vidicon detector capable of measuring weak optical signals, a set of 2 inch square ORIEL calibrated metallic neutral density filters were utilized. Neutral filters are specified by optical density which is a measure of the attenuation of the filter. It is defined as the base 10 logarithm of the reciprocal of transmittance. Hence a filter with optical density of 1 transmits 10% of the light incident upon it. It is also obvious that the optical density of a stack of filters equals to the sum of the optical densities of each individual filter. Thus, intermediate values of densities can be obtained through combinations of neutral density filters.

Emission intensities are different at different axial (vertical) positions of the plasma. Optical density of the filter has to be changed accordingly. Previously this was done manually, which inevitably interrupted the fluency of data acquisition. Later a solenoid driven neutral density filter controller was built which allow automatic insertion and removal of filters. Four filters of optical densities: 0.5, 1, 2, and 3 were used which could combine to give densities from 0.5 to 6.5 with an increment of 0.5. Each filter is mounted on an aluminum rod which is linked to a selenoid by a spring. When the selenoid power switch is turned on, the corresponding filter is put into the light path. The filter-selenoid assembly is enclosed in a 13x16x23 cm light weight aluminum box which is mounted on the optical rail near the monochromator entrance slit.

As demonstrated in Figure 3.4, a "slice" of the plasma image enters the

monochromator entrance slit. The grating then expands the image of the slit spectrally in the direction perpendicular to the slit. This forms a two dimensional optical output with one dimension corresponding to the plasma radial position, and the other the wavelength. This 2-D image is then projected to a vidicon detector surface where optical signal is converted to electric voltage and further digitized and stored for data reduction.

3.3.2 Optical Multichannel Analyzer

The EG&G Princeton Applied Research OMA III system consists of three parts: the Model 1460 OMA Console, the Model 1216 Multichannel Detector Controller and the Model 1254 Silicon Intensified Target (SIT) Vidicon Detector.

The console is the center unit controlling data acquisition, display and storage. Update software packages are provided by EG&G PARC using the keyboard and/or touch screen. Various data acquisition modes and scanning sequences are available which include live, live minus background and accumulated intensities. It also has a gated mode which requires the use of a Model 1211 High Voltage Pulse Generator. Data will be immediately displayed on its 9 inch screen and stored in either a 20 MB hard disk or a 150 K floppy disk. The console can talk with other devices such as a printer, a plotter or another computer through the RS232 ports.

In the summer of 1987, some data storage problems occurred which had been solved by replacing the console's I/O-A board and the hard disk.

The 1216 Multichannel Detector Controller serves for two purposes. First it accepts the scanning code from the console and drives the vidicon scanning sequence. Second it receives and digitizes signal from the vidicon and send it to the console for display and storage.

The SIT vidicon has a 12.5x12.5 mm detector surface composed of 512x512 pixels.

These pixels can be grouped in different patterns and be exposed for different time intervals. The parameter changes are made through the OMA console. The vidicon is a light integrating device. Charge stored on the capacitance of each detector element is depleted by incident photons and thermally freed electrons. At the end of the exposure (integration) period, the target is scanned by an electron beam that recharges the target elements. The variation in beam current as the target is scanned becomes the signal that is digitized in the detector controller. The vidicon has a sensitivity of approximately 2 detected photons/count with a linearity of $\pm 2\%$ but is a function of intensity. Useful spectral range starts from 365 nm to 800 nm and can be extended down to 200 nm with a UV scintillator coating. The sensitivity curve can be found in Figure 3.5.

3.3.3 Translation Stage and Stepping Motor-Controller

The plasma imaging optics, the monochromator and the vidicon are all mounted on a vertical translation stage, so that the whole assembly can be moved up and down to map out the entire plasma region "slice by slice". This vertical stage then sits on another translation stage which provides horizontal movement of the detector system. This is particularly useful in catching the plasma and locating it at the center of the vidicon surface.

The translation stages are constructed from Velmex UniSlide rails and Superior Electronic stepping motors. They are controlled by a Velmex 8300 Series Control/Driver and a Tandy TRS-80 DT-100 Monitor through a short BASIC program.

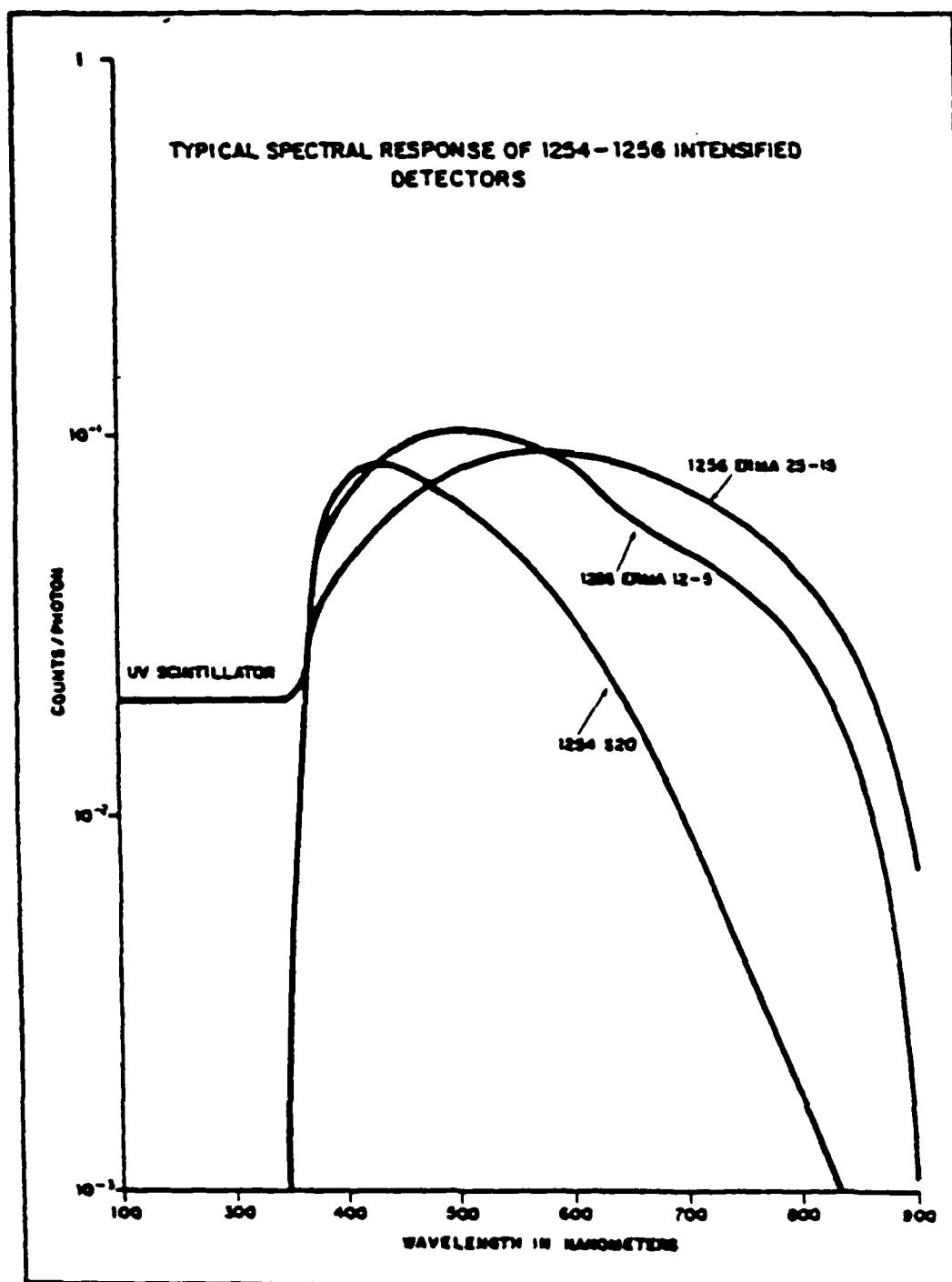


Figure 3.5 Spectral response curve of the silicon intensified target.
(From the OMA manual)

Chapter 4: Experimental Procedure and Data Analysis

This chapter is intended to be a guideline of doing spectroscopic diagnostics of laser-sustained plasmas. All the experiments reported here were done with CW CO₂ laser-sustained argon plasmas, and were carried out in the Materials Engineering Research Laboratory (MERL) laser room located in the Talbot Laboratory. However, one should find it very helpful to follow the experimental procedure outlined in this chapter, whenever the OMA system is put in use as an optical diagnostic means.

System alignment is the first and the key procedure for obtaining reliable experimental results, and thus could not be over-emphasized. Normal data acquisition procedures are described following a brief explanation of the OMA system operations. Then the incident laser beam is analyzed to acquire beam profile necessary for absorption calculations. Finally the data reduction procedure is detailed in its own sequence: the calculations of electron temperature, total plasma absorption and radiation loss, and the system thermal efficiency.

4.1 Alignment

This is a very crucial part of the experiment to which a lot of attention and patience should be given. Once the alignment is achieved, the data acquisition will continue for days. The reliability of the data taken depends heavily on the system alignment. The procedure can be divided into two steps: the alignment of the plasma imaging optics, and then the monochromator and the detector head. Normally it takes two to three hours to do the system setup and alignment.

4.1.1 Alignment of Plasma Imaging Optics

The plasma imaging optics consists of a plano-convex lens, a lens holder and an optical rail. It is used to focus the laser-sustained plasma onto the monochromator entrance slit. The purpose of the alignment is to achieve a sharp image of the plasma which underfills the slit width, and to make sure that the imaging f number matches the monochromator f number. Also checked is whether the optical axis is horizontal.

First the focal point of the CW CO_2 laser must be found. This is done by taking plexiglass burns with short pulses of sub-kilowatt laser power. A plexiglass plate of 1/8 inch thickness is put near the focus to burn a hole. The hole gets smaller as the plate approaches the laser focus, and becomes larger as it gets further away from the focus. The plate position where the hole size is at the minimum indicates the laser focus position. This is believed to be accurate to within 1 mm.

In most CO_2 lasers, there is an HeNe beam which simulates the real laser beam path. This can be used to determine the focal point only when the laser focusing optics consists solely of mirrors. Whenever a lens is involved, however, the method is not valid anymore, because the HeNe and the CO_2 laser have different frequencies, thus different indices of refraction for the lens material and different focal lengths. A sodium chloride lens of 21 inch focal length for the $10.6 \mu\text{m}$ CO_2 laser was found to have about 1 inch longer focal length for the 632.8 nm HeNe laser.

Once the laser focus is determined, A HeNe laser beam is sent from the other side of the gas flow chamber through the laser focal point, as shown in Figure 4.1. The Uniphase Model 1508P 0.95 mW HeNe gas laser was used for this experiment. The HeNe laser is put on two small jack stands. Fine adjustments are made so that the HeNe laser beam propagates horizontally, which is checked by holding a level close to the beam path. This HeNe beam will serve as an important reference tool and should not be moved until the alignment is finished.

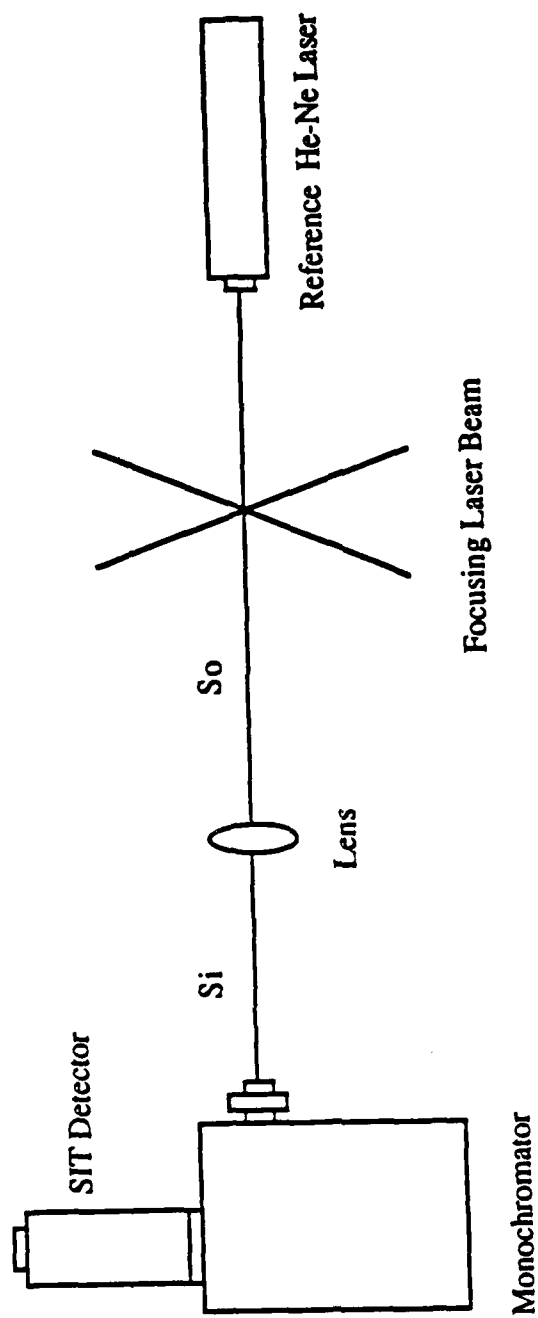


Figure 4.1 Alignment of plasma imaging optics, monochromator and vidicon detector.

Now is the time to assemble the OMA, the monochromator and the stepping motor driven stages (refer to Figure 3.3). Leave the OMA power off but turn on the stepping motor controller and switch it to manual control, so that the two stages can be moved continuously through manual control. The whole system sits on the horizontal stage which must be mounted on a stable table. The distance between the detecting system and the plasma object is determined after the following considerations.

First, the distance between the lens and the plasma object S_o , the distance between the lens and the monochromator entrance slit S_i , and the focal length of the lens f must obey the following equation:

$$\frac{1}{S_o} + \frac{1}{S_i} = \frac{1}{f} \quad (4.1)$$

in which the subscripts o and i stand for object and image respectively.

Second, the plasma image has to be small enough in radial dimension so that it underfills the monochromator entrance slit which is 8 mm long. Also the detector response gets worse at the edges, thus it is recommended to limit the image to the central region of the detector face. These come down to a proper image size of $D_i < 5$ mm in radial dimension. The real plasma diameter D_o is usually 10 mm to 15 mm in the argon gas case. Hence the optical magnification gives another relation as:

$$\frac{S_i}{S_o} = \frac{D_i}{D_o} = \text{Optical Magnification} \quad (4.2)$$

in which D_i and D_o are known.

Therefore, S_i and S_o can be obtained by solving equations (4.1) and (4.2) simultaneously. And the detecting system can be put in such a position that the

monochromator entrance slit is $S = S_i + S_o$ away from the laser focus point.

Without the lens, the two stepping motor driven stages are controlled manually to position the monochromator, so that the HeNe reference beam passes through the center of the entrance slit. Be careful not to turn on the OMA because the HeNe beam can cause serious damage to the vidicon detector. At this moment, it is necessary to make sure that the vertical stage is indeed vertical to ensure vertical translation of the detector in later data acquisition.

Mount the plano-convex lens on the lens holder which is attached to the optical rail. The curved surface of the lens should face the side with less beam bending, which, in this case, is the side of the plasma. The lens should be put in a position decided by the solutions of equations (4.1) and (4.2). Fine adjustments on the lens holder enable the HeNe reference beam to pass through the center of the lens and be focused on the center of the monochromator entrance slit, the same spot the HeNe beam reaches without the lens.

Now we have reached a point where the laser focus and the monochromator entrance slit are on the horizontal optical axis of the lens, and the relative positions of the three are such that proper image of the plasma should be observed at the entrance slit. Further adjustment of the imaging optics is made through the use of a neon spectral lamp at the CO_2 laser focal point. The spectral lamp has a U-shaped discharge tube. It is recommended to put the U-shape toward the lens so that one has a double line as an image. By observing the image of the spectral lamp at the entrance slit while moving the lens holder back and forth along the optical rail, one can find the best position of the lens which generates the sharpest image. Then the lens holder is tightened on the rail.

The last thing that needs to be taken care of is the matching of the plasma imaging f number with the monochromator f number. It is required by the internal

optics of a monochromator that light has to enter its entrance slit in a certain f number. Reference [25] describes the calculation of the monochromator f number, which gives a result of $f/4.96$ for the 415.8 nm ArI line. Hence the diameter of the lens aperture d has to be limited so that the following relation be satisfied:

$$\text{Monochromator } f/\# = \text{Plasma Imaging } f/\# = \frac{S_i}{d} \quad (4.3)$$

Usually the lens diameter is larger than required to match the f number. Thus some of the outer edge of the lens has to be blocked. This is achieved by placing a shutter of proper diameter d in front of the lens, or simply cut a hole in an aluminum foil which is then wrapped on the lens.

4.1.2 Alignment of Monochromator and Vidicon Detector Head

After the plasma imaging optics, a "slice" of the plasma image enters the monochromator slit and is expanded spectrally, giving an output of two dimensional image which is picked up by the silicon intensified target vidicon detector head.

The internal optics of the monochromator is rather delicate and the alignment requires professional skill. However, since its components are kinematically mounted against vibration, it should remain in good condition for a long time if operated with care.

The monochromator is set in such a position that its entrance slit is horizontal, while the output port is facing up vertically. The reference HeNe laser beam should enter through the slit and come out at the center of the output port, if the wavelength dial is set to 632.8 nm with the 1200 grooves/mm grating used. Further checking can be made by putting a mercury spectral lamp at the entrance slit and observe the spectral lines at the exit port while changing the wavelength dial. To

avoid eye exposure to the ultraviolet radiation, one can use a piece of white paper as a diffuse screen.

The alignment of the vidicon detector head is namely to find the right position to put it on top of the monochromator exit port. The monochromator, being nothing else but an optical device, has a certain location outside its exit port where the output image is sharply focused. We call it the monochromator focus plane. One will see clear spectral lines (images of the slit at different wavelengths) on a screen at this plane. It was told by the manufacturer that this focus plane is at approximately 34 mm away from the exit port.

Therefore, it is essential to set the vidicon in such a position that the detector surface is at the monochromator focal plane. It is noted that the active detector surface, the pixel array, is 0.38 inch inside the protective window. Hence the relative distance of the vidicon and the monochromator can be estimated.

The ultimate alignment, however, is made through the use of the OMA. The emission of a neon spectral lamp at the laser focal point is observed by the OMA in its "live" mode. A neutral density filter of optical density 2 is needed to cut down the intensity to a safe level. The SIT vidicon detector is mounted by three screws onto an OMA adaptor which can be glided in or out of the monochromator exit port. Neon spectral lines of highest intensity should appear when the OMA adaptor is moved to the right position where the detector surface coincide with the monochromator focal plane.

The same procedure can be repeated with an argon spectral lamp, but no neutral density filters are necessary due to its low intensity. Be sure, however, to change the monochromator wavelength dial to the argon line wavelength of 415.8 nm, which is the spectral range of interest in this experiment.

4.2 OMA Operations

All the functions of the OMA system are controlled through the Model 1460 console. The various OMA manuals provide detailed information about its operations. This section highlights the frequently used functions during this investigation, which will be further discussed in the sections that follow whenever they are encountered.

Data acquisition mode can be chosen among live, live-B and accumulative modes. The live mode continuously updates the signal it receives and shows it on the screen. The live-B mode works the same as the live mode, except that it shows the background subtracted signals. The background signal, of course, has to be recorded without the plasma prior to data acquisition. The accumulative modes are used to accumulate tens to thousands of data scans in a controlled sequence programmable through the console. The most frequently used is the data acquisition mode #6, which is a simple addition of intensities of subsequent data scans with prep scans in between to "cool off" the detector.

Figure 4.2 illustrates how the vidicon surface is arranged for data acquisition. The two dimensional detector surface consists of 512x512 pixels. The direction corresponding to the spectral spread is denoted as X axis, and the other as Y axis corresponding to the plasma radial dimension. The range of the parameters X and Y is then naturally from 1 to 512. However, because of the drop off in response at the outer 10% of the detector surface, X and Y are usually limited to the central region.

The X parameter is otherwise called "channel". The beginning and end of the X parameter can be changed by setting X0 and number of channels, the end of X being $X0 + (\# \text{ of channels})$. This enables the experimenter to manage the spectral range to be scanned.

The pixels in the Y direction have to be grouped in "tracks" with a minimum of 5 elements in each track to eliminate error. The beginning of the Y parameter is

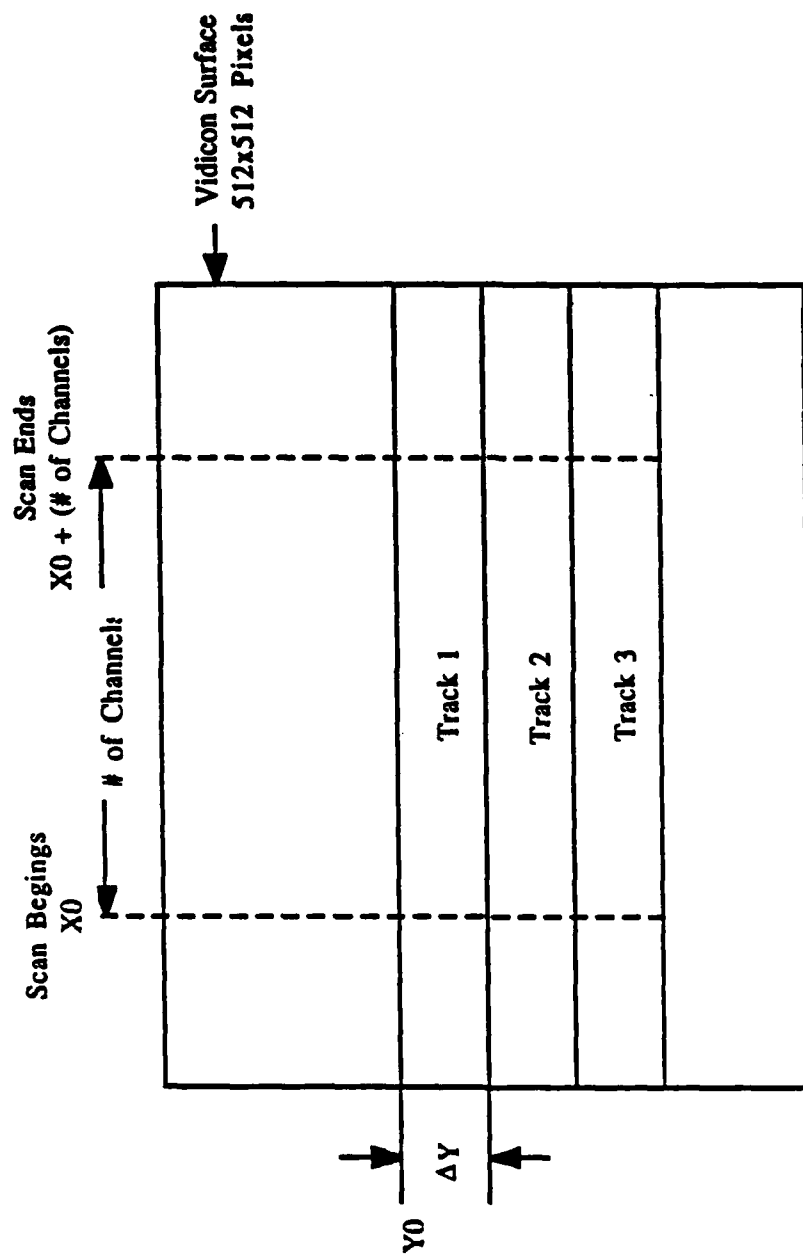


Figure 4.2 Schematic showing the vidicon surface arrangement changeable through OMA console.

selected by Y_0 , the track width by ΔY . Also specified is the number of tracks. Hence, the range of Y is from Y_0 to $Y_0 + \Delta Y$ (# of tracks).

Channel time is the time interval during which a scanned channel is exposed to the light signal. It is variable between 20 μsec and 140 μsec . With the strong signals that we had from the plasma emission, the shortest channel time was used. Consequently, track time and frame time are the time intervals during which one track or the whole scanned area is exposed to the light. When using the accumulative data acquisition mode, the experiment time indicates the time necessary to scan and add a series of exposures and preparation scans, the pattern of which is previously programmed. For a typical laser-sustained argon plasma, experiment time is 4 to 9 seconds.

Since the silicon intensified target vidicon is designed as a highly sensitive light detector, too strong light intensities can cause saturation or even permanent damage to the detector. It is our experience that, with the minimum track width of $\Delta Y = 5$, ten accumulated data scans should not exceed a total count of 10,000. In other words, if the live mode is used, the count for each track must be less than 1,000. Neutral density filters are placed in front of the monochromator entrance slit in order to reduce light intensity. Optical densities of 0.5 to 5.0 were found necessary for different vertical positions of the laser-sustained argon plasma. Specifications and control of neutral density filters are featured in Section 3.3.1.

Once a satisfactory data is obtained, it can be assigned a file name and stored in either the hard disk or a floppy disk. The OMA system is capable of doing the first few steps of data reduction, such as channel profile (integration) and curve calculations.

4.3 Finding the Plasma

After doing the alignment and getting acquainted with the OMA operations, here comes the real thing: taking plasma emission spectra with the system. The first and probably the most difficult step, however, is to find the plasma, or in other words, to locate the image of the plasma onto a desired area of the vidicon surface.

In the alignment of the plasma imaging optics, the optical axis of the lens coincides with the reference HeNe laser beam which is set horizontal to a vertical level so that it passes through the CO₂ laser focus spot. Therefore the slice of the plasma image entering the monochromator slit corresponds to the slice of the plasma at the CO₂ laser focus. This vertical position is marked as $Z = 0$. Since exact vertical positions are essential in later data reduction, it is important not to change the vertical position of the monochromator/detector assembly when trying to find the plasma through the OMA.

All the plasmas are sustained in a region around the CO₂ laser focus. With a plasma initiated and sustained in a steady state, the monochromator/detector assembly is moved horizontally through manual control of the horizontal translation stage, until it comes to a position where the plasma is imaged right on the monochromator slit. The OMA will show the strongest argon emission lines in its live mode.

It is obvious that, at the CO₂ laser focus, the plasma will be cylindrically symmetric, with emission intensity peaking at the center and gradually diminishing along the radius. The vidicon surface has to be divided into at least 10 tracks to reveal this trend, which is demonstrated in Figure 4.3. The OMA screen shows only one track of a multiple track data in the data acquisition mode. To see a complete picture like Figure 4.3, one need to get in the X-Y plot mode. Generally the outer 10% of the vidicon surface is avoided, beside others such as previously burned spots in the detector.

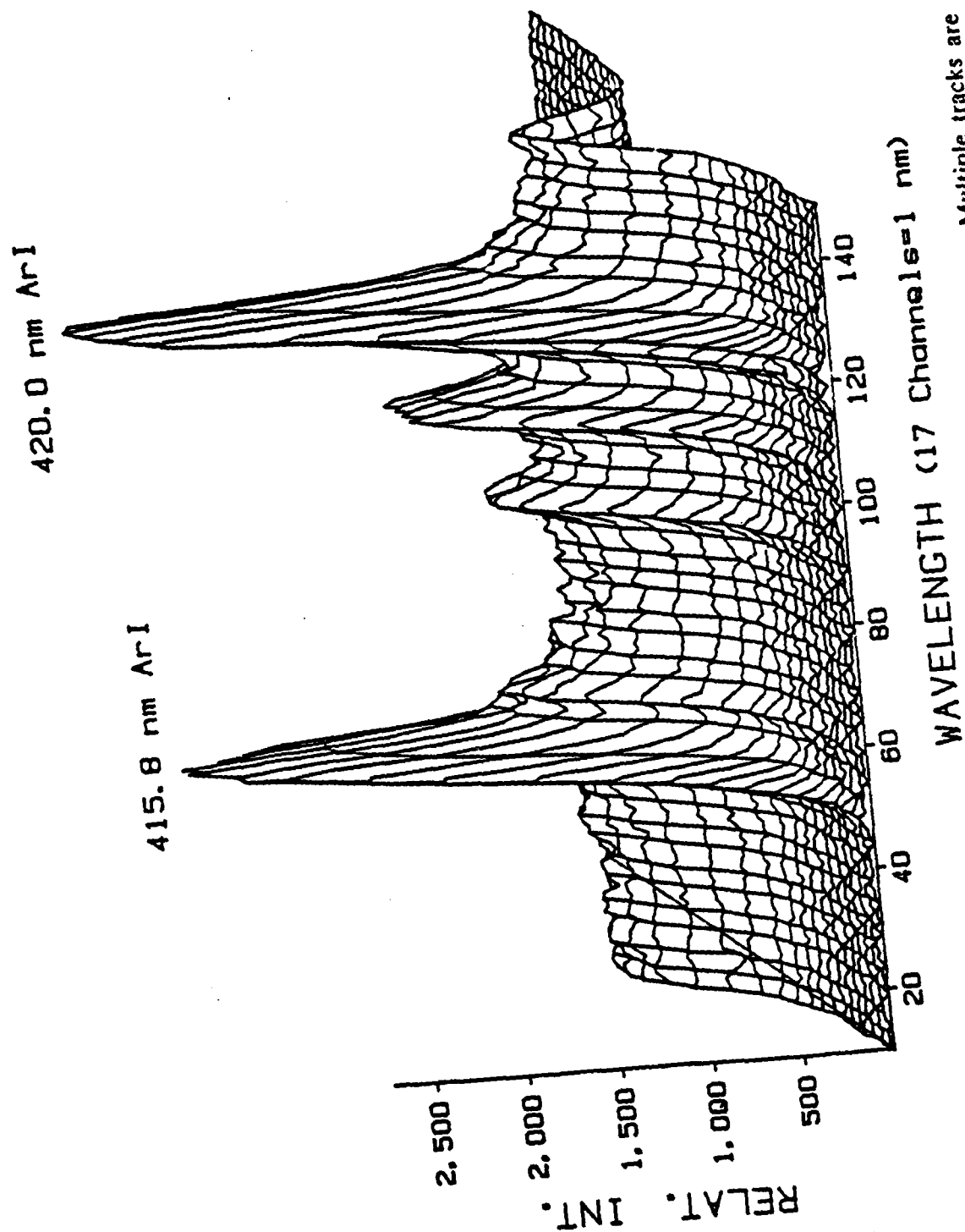


Figure 4.3 A typical data file as appeared on the OMA screen. Multiple tracks are used which correspond to different radial positions across the plasma.

By taking data at slightly different horizontal positions, the best location can be found where the plasma is well imaged in the best region of the vidicon surface. The monochromator/detector assembly should be kept in this horizontal position throughout the experiment. Only the vertical position is allowed to vary in order to map out the entire plasma volume.

4.4 Data Acquisition

All the data acquired in this experiment used the OMA data acquisition mode #6, in which intensities from subsequent data scans are added with several preparation scans in between. The preparation scans are detector scans without light exposure, which are intended to eliminate dark signals. The number of added and preparation scans are all set to 10.

The monochromator center wavelength was adjusted to 422.0 nm through the dial. In regard to the wavelength range detected, X0 was set to 100, and the number of channels 150 (refer to Figure 4.2). This range is large enough to include the 415.8 nm and 422.0 nm ArI lines. The least necessary range was chosen to speed up the data acquisition process. Channel time was also picked as 20 μ sec, the shortest available. 40 tracks were selected with $\Delta Y = 5$ and $Y0 = 180$. This was proven to be adequate to catch the entire radial extension of laser-sustained argon plasmas.

A plano-convex lens of 20 cm focal length was used. Distances from the lens to the plasma and to the monochromator slit were measured to be $S_0 = 792.4$ mm and $S_1 = 258.0$ mm, resulting in an optical magnification of 0.3256. Slit width of 0.025 mm was used.

The vertical translation stage was controlled through a BASIC program (see Appendix A). It enables the monochromator/detector assembly to move up or down in equal step sizes. Vertical increment of $\Delta Z = 2$ mm was used in this experiment.

One data was taken at the original vertical position $Z = 0$, and was stored in the OMA hard disc. Then the vertical stage was moved up or down by ΔZ to take another data. This process went on until the end of the plasma was reached. Then the vertical stage was brought back to the $Z = 0$ position and started moving and taking data in the other direction.

One can also start from one end of the plasma to the other. But often it takes time to find the "end" of a plasma, because one cannot tell confidently until the line-to-continuum ratio is examined. One easier indication, however, is that the intensity distribution among the tracks tend to be flat when the end of a plasma is approached. The intensity peak that shows the center of the plasma no longer exists.

The flow chamber was heated by the radiation from the plasma. Normally after continuous data acquisition of 5 to 8 minutes, the chamber temperature would get as high as 450 K. A 20 minutes waiting period was necessary for it to cool down. One complete data set of a plasma requires 2 or 3 such continuous sessions.

4.5 Laser Power measurement and Beam Analysis

Laser power was measured with a Series 25 Laser Power Probe made by the Optical Engineering, Inc. Due to different laser power losses for different lenses and mirrors, the power that actually reaches into the plasma chamber was measured for individual case. This is done by placing the power probe inside the chamber prior to plasma experiments. Details are documented in Reference [14].

In order to calculate total absorption and thermal efficiency, the laser beam geometry must be determined. This is accomplished by measuring beam profile near the focus and far away from the focus.

Beam profile near the focus was measured by the Laser Beam Analyzer (LBA). For this purpose, the gas chamber has to be taken out and the LBA be placed at the

level near the CO_2 laser focus. In the LBA, a highly reflective needle is driven by a synchronous-motor to rotate in a plane perpendicular to the beam. As the needle crosses the beam, it reflects a fraction of the beam onto two detectors in such a way that, two signals proportional to the intensity distributions in two perpendicular cross sections are obtained. However, by the time the experiments were performed, one of the detectors was unable to be used due to previous damages.

The signals are then amplified and monitored by an oscilloscope. The oscilloscope used was a Type 1425 20 MHz Digital Storage Oscilloscope, which can store the signals for convenient photographing. On the oscilloscope screen, the voltage of the signal is proportional to the beam intensity, while the time axis is proportional to the location along the beam diameter.

To prevent saturation, the laser power has to be limited to less than 1 kW. A typical oscilloscope setting is an amplification factor of 20 mV/div and a time base of 0.05 ms/div. The conversion factor is that, 100 μsec in passage time corresponds to 2.12 mm in distance. By moving the cursor on the oscilloscope screen, the time interval between two points can be read to an accuracy of 0.5 μsec , which transports to 0.01 mm accuracy in position.

The CO_2 laser focusing lens was moved vertically by the FLUKE controlled precision stage described in Section 3.2. While keeping the LBA stationary, the lens was moved in steps of 2 mm, so that the beam profile near the focus can be mapped out. Figure 4.4 shows a result for the $f/7$ optics. The beam has a donut shape, which is represented by the two peaks on each side of the centerline. The diameter of the focal point can also be estimated from the beam profile, which is typically 1 mm for the $f/7$ optics.

To obtain the beam geometry far away from the focus, a plexiglass burn pattern can be taken some distance behind the focus. The inside and outside diameters of the

LBA ANALYSIS OF F/7 LASER BEAM

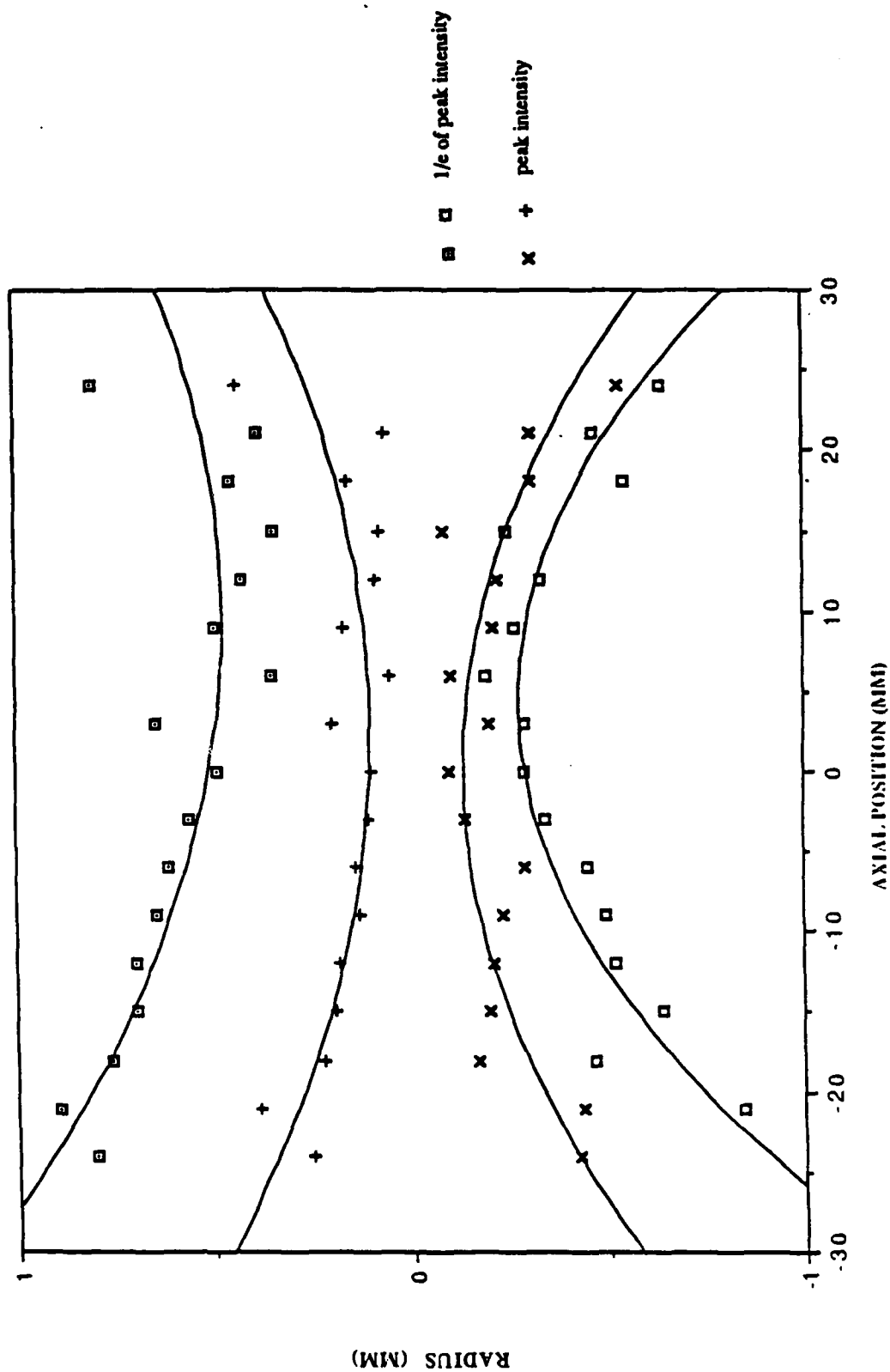


Figure 4.4 F/7 beam profile as measured by the LBA. Solid lines are second order curve fits.

donut-shaped burn pattern are measured. For the purpose of calculating total absorption, the details of which will be discussed in the next section, the angles of incidence of the inside and outside edges of the annular beam are determined. Then the beam is divided into 20 cone-shaped rays as illustrated in Figure 4.5, where straight line propagation is assumed for each ray. Therefore angles of incidence of every ray are determined.

4.6 Data Reduction

The first data reduction process is the preliminary reduction on the OMA console, which generates the 415.8 nm ArI line and continuum intensity distribution files. The files are then sent to the HP-9000 computer for further process which yields the temperature distribution, the total absorption and thermal efficiency.

4.6.1 Preliminary Data Reduction on OMA

The Model 1460 Console of the OMA system provides some useful data processing functions such as "channel profile" and "curve calculation". Channel profile allows intensity integration over a specified channel (wavelength) region, which generates a single curve showing the integrated intensity versus the track number (radial position). The curve calculation function is a point-to-point mathematical computation such as addition, subtraction, division, multiplication, etc..

First the background signal was subtracted from the data utilizing the curve calculation function. A background file was acquired and stored in the OMA without a plasma. It was found that the background was dominantly dark signals of the detector itself. It existed even when the detector was covered. Therefore variations in background intensity was minimal, and only one background data was necessary for the entire set of data for one plasma.

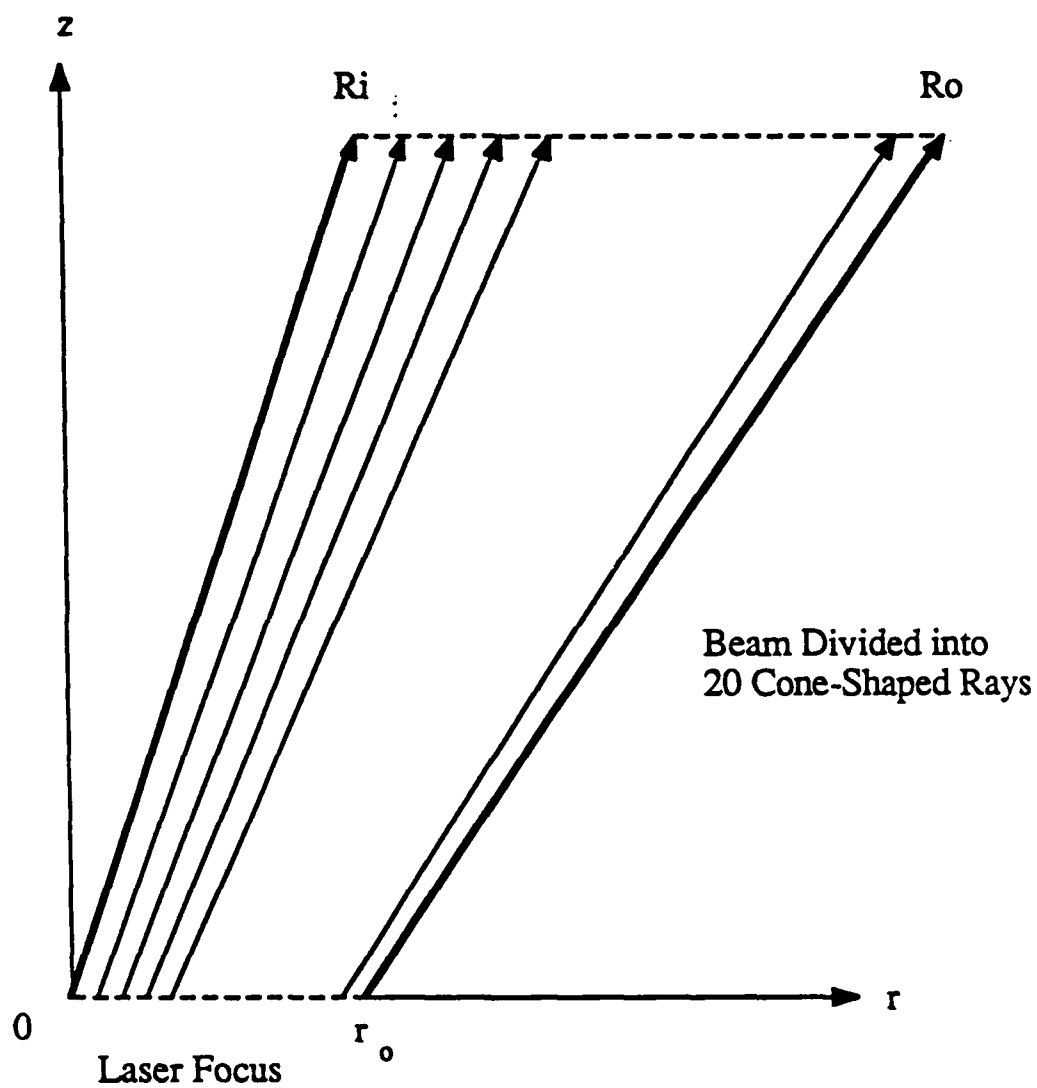


Figure 4.5 Propagation of the focused laser beam. Beam geometry is measured at focus and away from the focus to determine the angles of each ray.

415.8 nm ArI line and continuum intensities are what will be used for temperature determination. It was found [20], however, that using integrated intensities over the width of the spectral line yields better temperature predictions than using the peak intensity alone. A proper width of 10 Å was used for the 415.8 nm ArI line.

The wavelength axis on the OMA is represented by channels. To find out how many channels is an equivalence of 10 Å, a data must be taken with a spectral lamp which has sharp peaks of known wavelengths. By moving the cursor on the OMA screen and read the corresponding channel numbers, the number of channels between two peaks is determined, which then gives the number of channels for a 10 Å interval based on proportionality. Usually there were 17 channels for our settings.

Using the channel profile function of the OMA, two intensity integrations were made. First was an integration over a 10 Å region around the 415.8 nm ArI peak. Beginning and end of integration were evenly chosen on two sides of the peak. This generated a curve which represented the addition of line and continuum intensities, $I_{\lambda} + I_c$. Then an integration of 10 Å range adjacent to the peak was taken, which yielded the continuum intensity I_c alone. Then the two files were subtracted to give the pure line intensity I_{λ} . The ratio I_{λ}/I_c was then calculated, also through the use of curve calculation function. Figure 4.6 is a typical set of line intensity I_{λ} , continuum intensity I_c and the ratio I_{λ}/I_c curves.

It is not surprising to see intensity peaks at the center of the plasma where temperatures are expected to be the highest. The line-to-continuum ratio, however, has a minimum at the center, which is explained by Figure 2.5 that smaller line-to-continuum ratio corresponds to higher electron temperature. The intensity curves in Figure 4.6 also shows the cylindrical symmetry of the plasma, with some deviations due to the nonuniformity of the CO₂ laser beam.

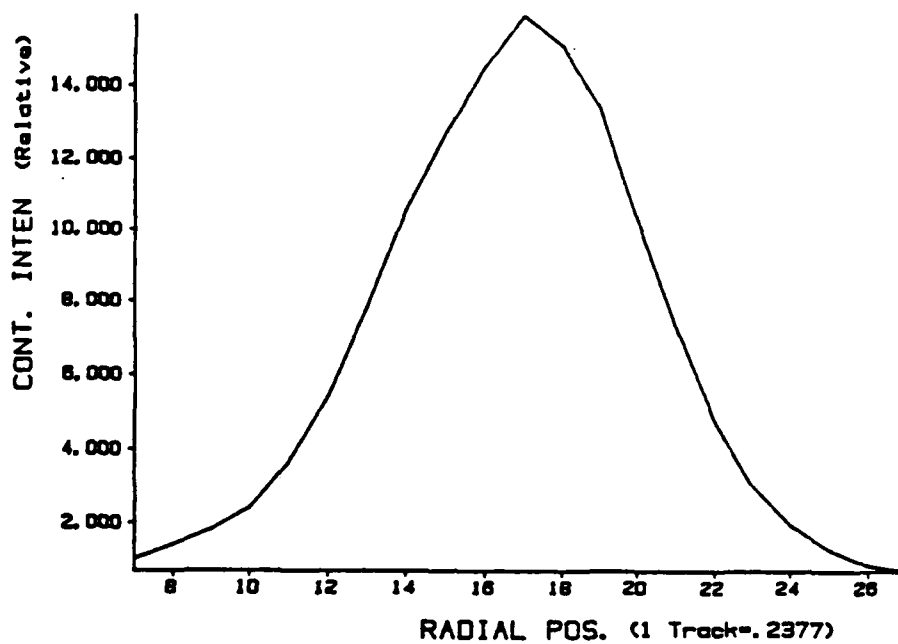
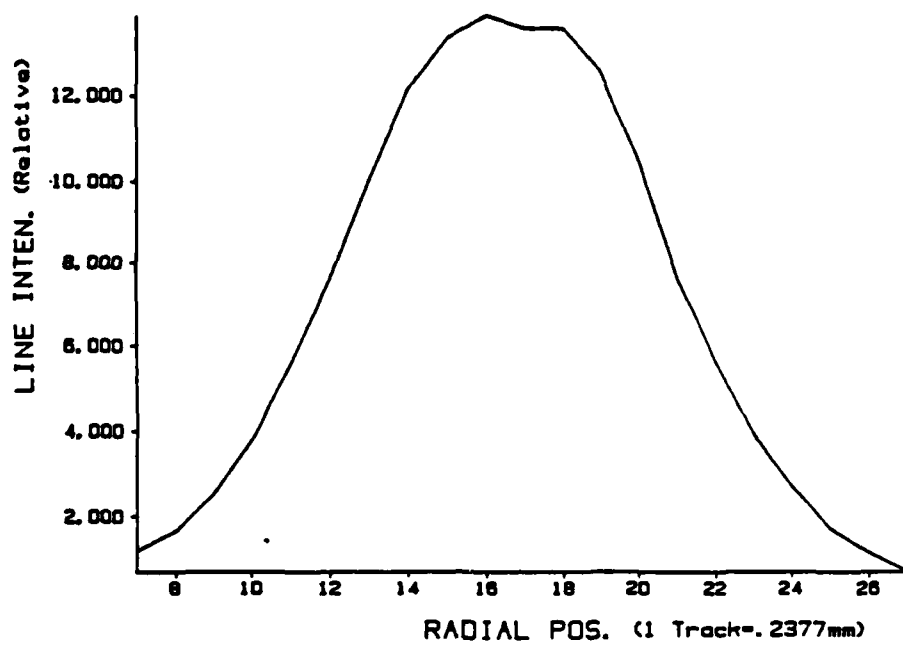


Figure 4.6(a) Line and continuum intensity curves after "channel profile".

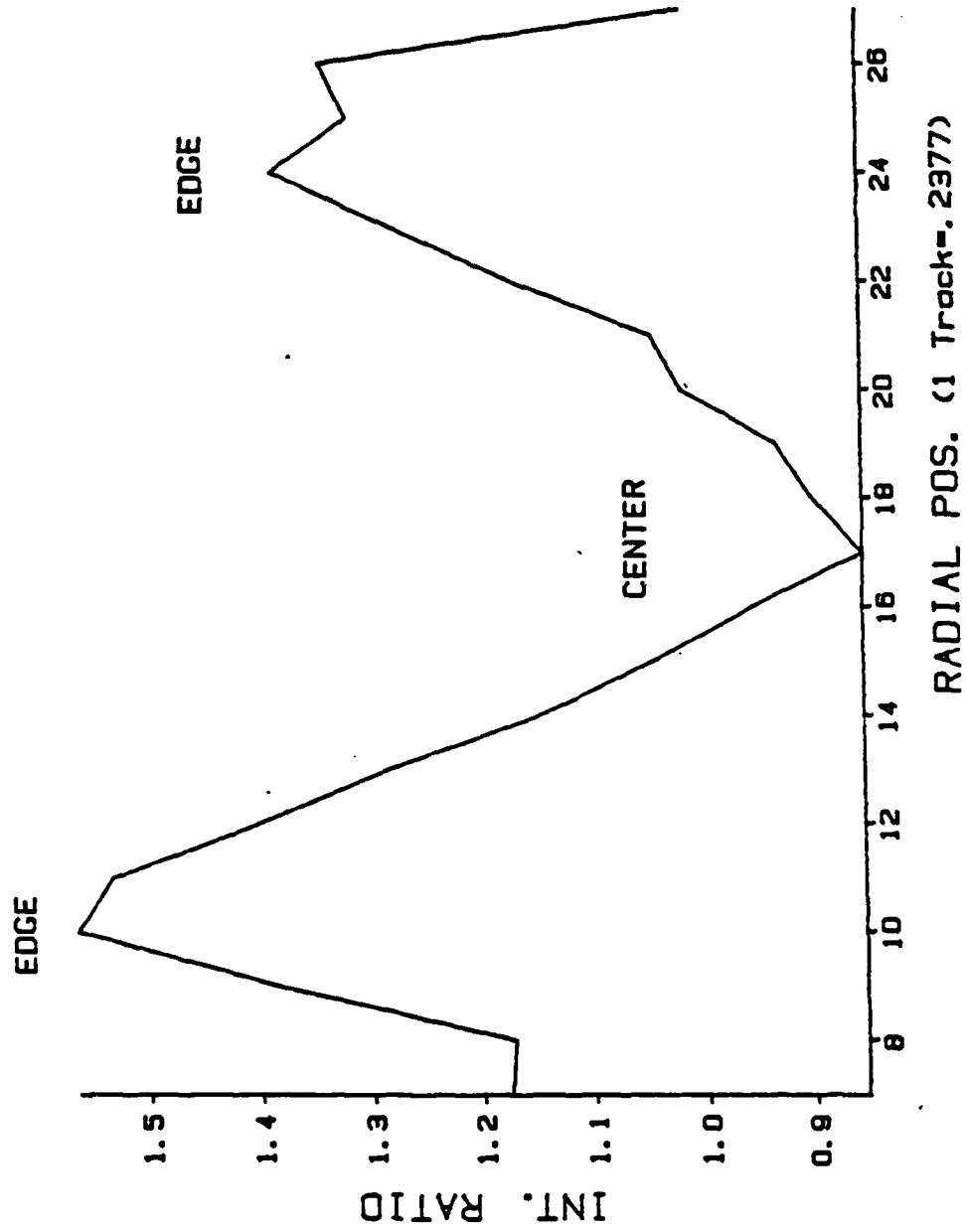


Figure 4.6(b) Line-to-continuum ratio by curve calculation. Smaller ratio indicates higher electron temperature. The outer edge of the data file has to be cut off.

It is noticed in Figure 4.6 that the ratio I_λ/I_c drops after a certain radial position (track number). The reason is that the temperature there becomes so low ($< 9,000$ K) that continuum radiation begins to dominate. Therefore the spectroscopic technique is no longer valid to predict the temperature, and the corresponding outer most data points must be eliminated. It should be pointed out that the ratio I_λ/I_c obtained from curve calculation is not the one used for temperature calculation yet. But it does tell the trends and is used to determine the plasma centerline and outer edge.

4.6.2 Abel Inversion and Temperature Determination

The intensities measured by the OMA are of line-of-sight integrated emission, which need to be inverted into local emissive power before being applied to the temperature calculations. Equation (2.6) is a mathematical expression of the process called Abel inversion, in which a cylindrical symmetry is assumed for the plasma.

In most cases, plasma emission intensities appeared quite symmetric about its centerline (see Figure 4.6), hence one half of the curve was chosen for the inversion. Averages were used in a few occasions when the symmetry is not very good. Then the line and continuum intensity files were sent to the HP-9000 computer for further data reduction.

The grid size of the data field was specified before the Abel inversion. The vertical increment equals to the distance that the monochromator/detector is translated between adjacent data scans, which was $\Delta z = 2$ mm in this experiment. The radial increment Δr is the length at the position of the plasma that corresponds to the width of a track on the detector surface. The 512x512 pixels of the detector surface has a size of 10x10 mm, hence a track width of $\Delta Y = 5$ corresponds to a width of $(5/512) \cdot 10$ mm. Considering the optical magnification of 0.3256 (Section 4.4)

and the monochromator magnification of 1.2612 [25], the radial increment was calculated to be $\Delta Y = 0.2377$ mm.

The Abel inversion code from Reference [20] was used to obtain local emissive powers from both the line and the continuum data files. Then the ratio was compared with the theoretical results presented in Figure 2.5 to get the local electron temperature. The final result was a two dimensional temperature field $T(z,r)$, with z and r being the axial and radial positions respectively. Temperature contour plots were obtained using the DI-3000 software package. The contour plotting code is attached as Appendix B.

4.6.3 Absorption and Efficiency Calculation

Inverse Bremsstrahlung (IB) is the process responsible for the laser power absorption by the plasma. IB absorption coefficient is a function of electron temperature as shown in Figure 2.3. The CO_2 laser beam was divided into 20 rays, each having a slightly different angle of incidence determined from the beam analysis described in Section 4.5. Each ray propagated through the temperature field, and the amount of power absorbed was summed along the beam path on a point-by-point basis. Total power absorbed was then obtained by adding the contributions from all the 20 rays. Dividing the absorbed power by the incident laser power yielded the fractional absorption.

The total radiation loss, however, has to account for contributions from every point of the plasma. Hence it is an integration over the entire volume of the plasma. Again, the local radiation loss is a function of electron temperature (Figure 2.4) which has already been determined. Power retained by the flowing gas is then the difference between the absorbed and radiated power. System thermal efficiency is defined as the fraction of the incident laser power that was converted into thermal

energy of the gas.

A complete code listings that was used for the Abel inversion, total absorption and thermal efficiency calculations can be found in Reference [20]. The programs are currently stored in the HP-9000 computer.

Chapter 5: Results, Discussion and Recommendations

With the flow chamber modification, mainly the addition of the flow straightener and the quartz tube, plasmas with as high as 10 m/sec gas flow speed were able to be maintained. This expanded the previously available speed range [20] by almost 10 times, which is very significant in determining the optimum operating conditions.

A number of parameters can be varied in the experiment, the most important being the laser power, gas flow speed or mass flux, the gas chamber pressure and the beam focusing f number. The plasma temperature, total absorption and thermal efficiency are presented here for laser powers of 2.5 kW and 5.0 kW, and mean argon gas flow speed of 2 m/sec to 10 m/sec. Focusing beam f number and gas pressure are known to have effects on plasma properties, but the data presented here are of $f/7$ optics and 1 atmospheric argon gas pressure. Type of gas or gas mixture is another concern. However, all the experiments reported here were with pure argon gas.

5.1 Plasma Temperature Distribution

The electron temperature distributions of all the plasmas were plotted as isotherms. An error of $\pm 4\%$ was assessed for the temperature. Figure 5.1 is chosen to demonstrate the characteristics of the temperature field, where laser power is 2.5 kW, argon gas mean speed is 394 cm/sec, with an $f/7$ optics and 1 atmosphere chamber pressure. Plasma core temperatures are above 16,000 K in our operating conditions, with maximums as high as 20,000 K. A typical plasma has a tear drop shape about 5 mm in diameter and a few centimeters long.

As seen in Figure 5.1, the temperature gradient is larger at the plasma front than at the tail. At the front, the temperature usually raises from below 9,000 K to 16,000 K in less than 4 mm, while at the tail it takes a few centimeters for the

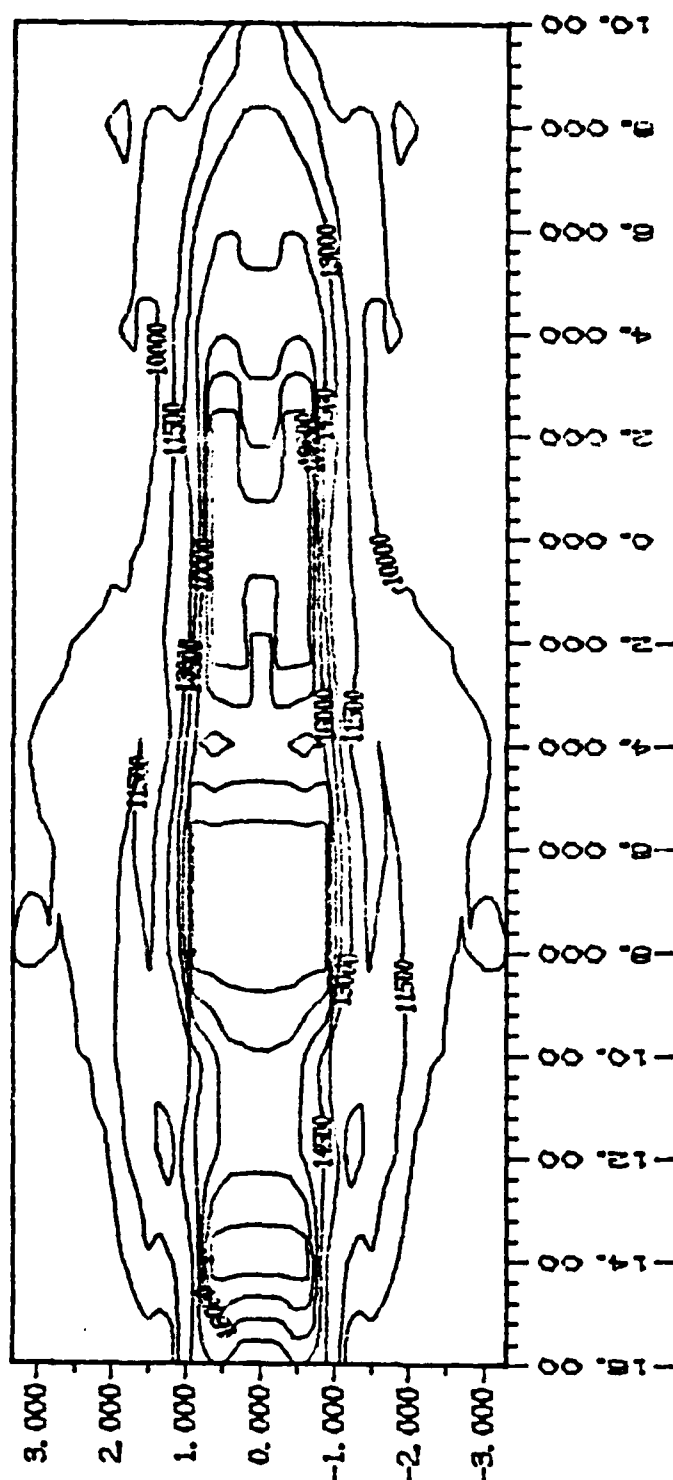


Figure 5.1 Electron temperature contour plot for an argon plasma with 2.5 kW laser power, f/7 optics, 394 cm/sec flow speed and 1 atmosphere chamber pressure.

temperature to drop back. This kind of geometry is the result of the gas flow. When cold gas flows and enters the plasma region, it gets ionized immediately and starts to absorb laser radiation through the inverse bremsstrahlung process. At the tail of the plasma, since most of the laser energy has already been absorbed, there is not as much ionization going on. Instead, it becomes a region of gas mixing which is elongated by the gas flow.

Because of the rapid temperature change at the plasma front, it is technically tricky to locate the exact beginning of the plasma region. It was done by examining the line and continuum intensity files I_λ , I_c , and their ratio file I_λ/I_c on the OMA screen. The sharp peaks, like those illustrated in Figure 4.6, will not appear until the plasma front is reached.

Also noticed in Figure 5.1 is the structure around the laser focal point, where the axial position is defined as zero. The two hot regions on both sides of the centerline is due to the fact that the CO_2 laser beam has a TEM_{01} * donut-shape profile. Hence it has a shape of a hollow cone when focused, and the corresponding plasma resembles the shape.

It is seen in Figure 5.1 that most of the plasma is upstream from the laser focus. This is true for plasmas of lower gas flow because it takes less power density to maintain a plasma at lower mass flux. When the flow speed is raised, the plasma tend to locate itself in a position closer to the focal point. However, when the gas flow gets so high that the laser power intensity can no longer sustain the plasma, it will distinguish. This is termed as plasma blow-out.

The trend of plasma being pushed downstream by higher flow rate is better illustrated in Figure 5.2 and Figure 5.3 for laser powers of 2.5 kW and 5 kW respectively, where the 11,600 K (=1 eV) contour lines are plotted for plasmas of increasing flow speed, and the positions of five plasmas are compared. It is believed

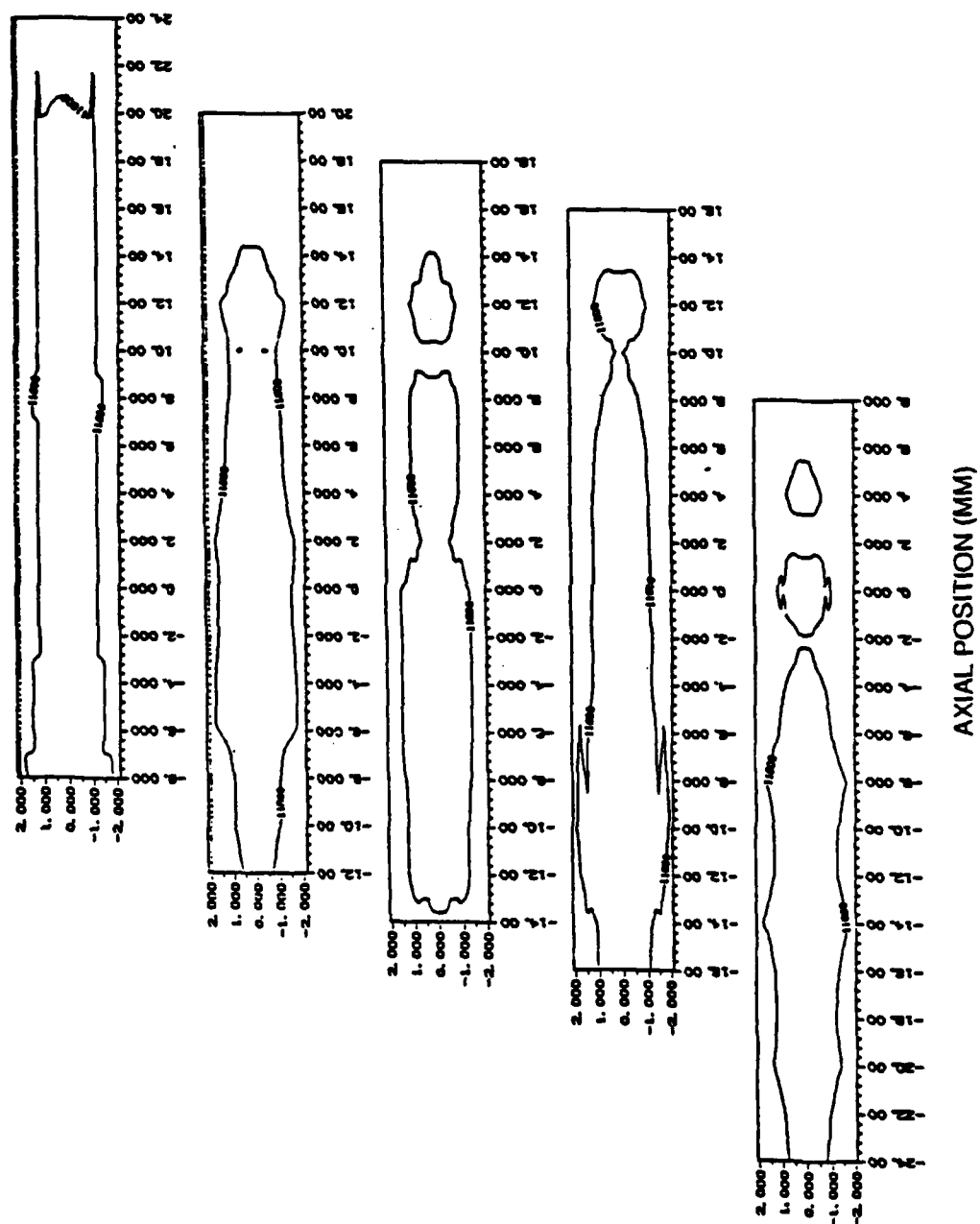


Figure 5.2 Relative position of 11,600 K temperature region. Axial position 0 corresponds to the laser focus. From below, the flow speeds are: 197, 394, 591, 788 and 985 cm/sec. Laser power is 2.5 kW.

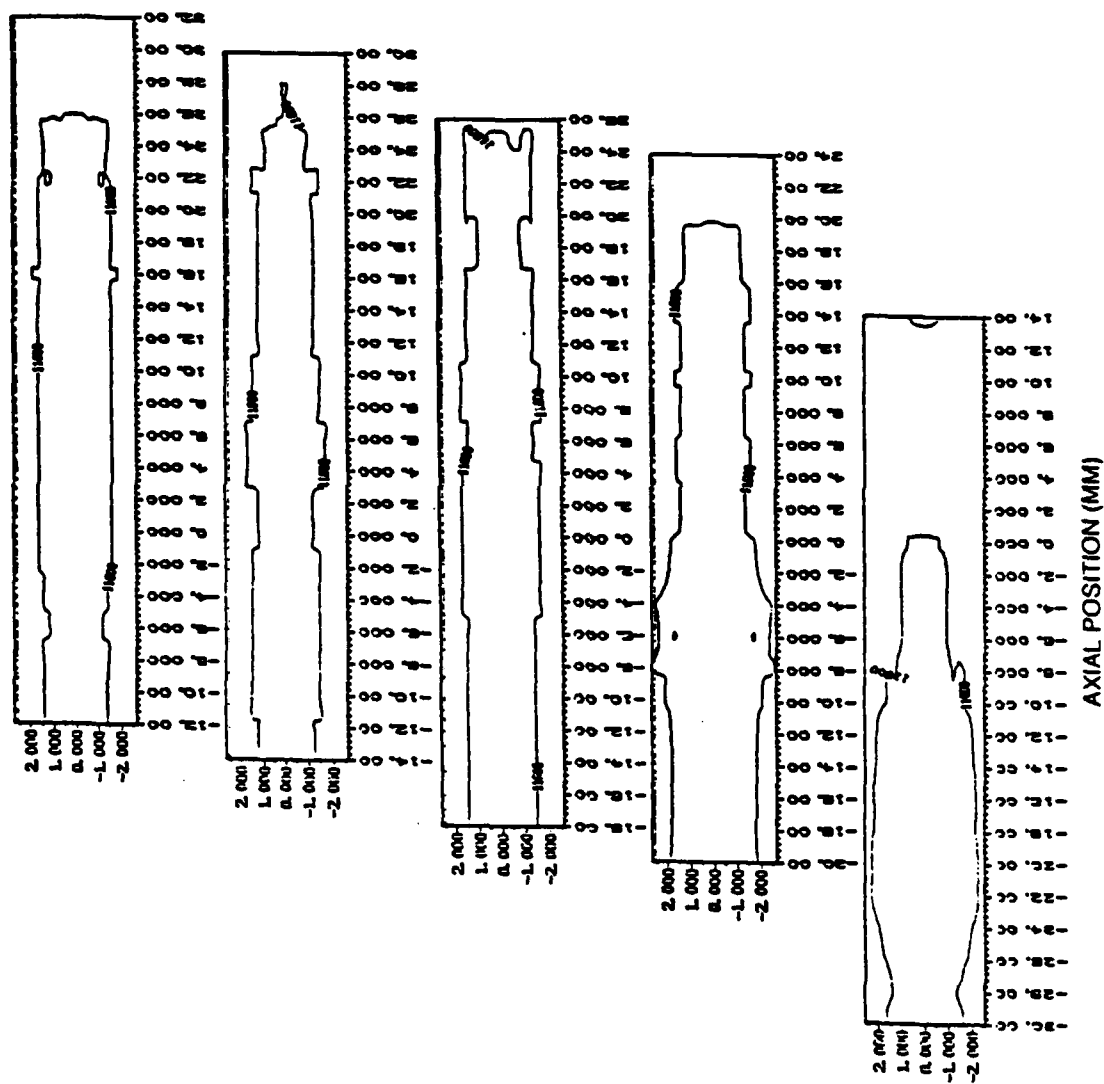


Figure 5.3 Relative position of 11,600 K temperature region. Axial position 0 corresponds to the laser focus. From below, the flow speeds are: 197, 394, 591, 788 and 985 cm/sec. Laser power is 5 kW.

that a plasma positioned around the laser focus will absorb more laser power, because that region has the highest power density which results in higher electron temperature and absorption coefficient.

The plasma core position, defined as the center position of the above 11,600 K region, is plotted against the flow speed for laser powers of 2.5 kW and 5 kW in Figure 5.4. Again, it demonstrates the effect of flow rate on the position of the plasma. The curves are second order curve fits of the experimental data.

Comparing Figures 5.2 and 5.3, one can see that the plasma front is further away from the focus with higher laser power. The plasma volume also becomes larger at higher laser power.

The length and radius of the 11,600 K region of a plasma are shown in Figure 5.5 and Figure 5.6 for different flow rate at two laser powers. It is understandable that the plasma size is always larger for the 5 kW laser power than for the 2.5 kW laser power. Also noticed is that, for both plasmas, when the length gets larger, the radius tends to be smaller, keeping the volume of the plasma relatively unchanged. One possible explanation is that, the plasma ionization rate depends on the laser intensity and gas number density, hence the plasma volume will tend to remain constant for the same laser power and gas pressure, while the change of gas flow rate will have effects mainly on the shape of the plasma. At present, however, no clear reasons have been found for the reverse trend of the 2.5 kW and 5 kW plasmas shown in Figures 5.5 and 5.6.

5.2 Total Absorption and Thermal Efficiency

It is believed that larger laser focusing f number will result in higher plasma absorption. The reason is that, as the f number increases, the plasma adjusts itself to the beam geometry and becomes longer and narrower. It allows the laser beam to

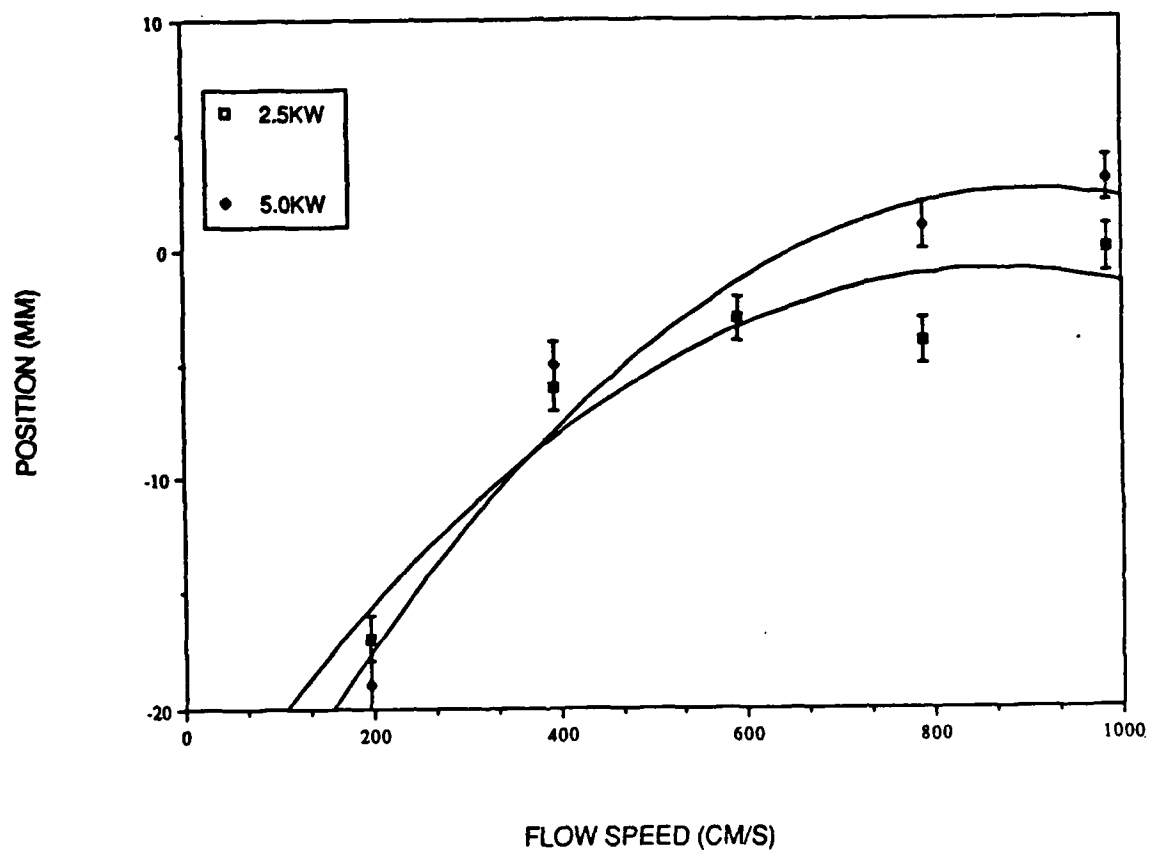


Figure 5.4 Plasma core position versus flow speed for laser powers of 2.5 kW and 5 kW. Position 0 indicates the laser focus.

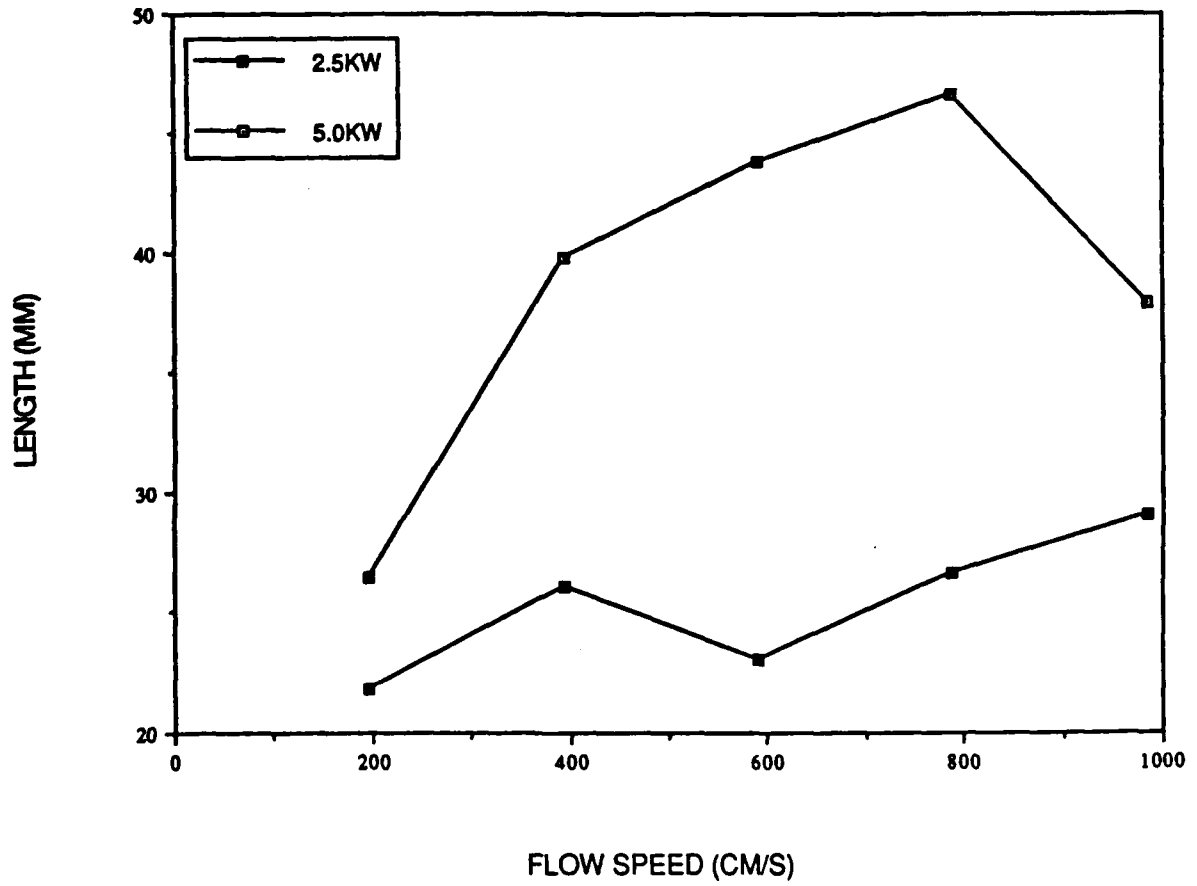


Figure 5.5 Length of the 11,600 K temperature region versus flow speed for laser powers of 2.5 kW and 5 kW.

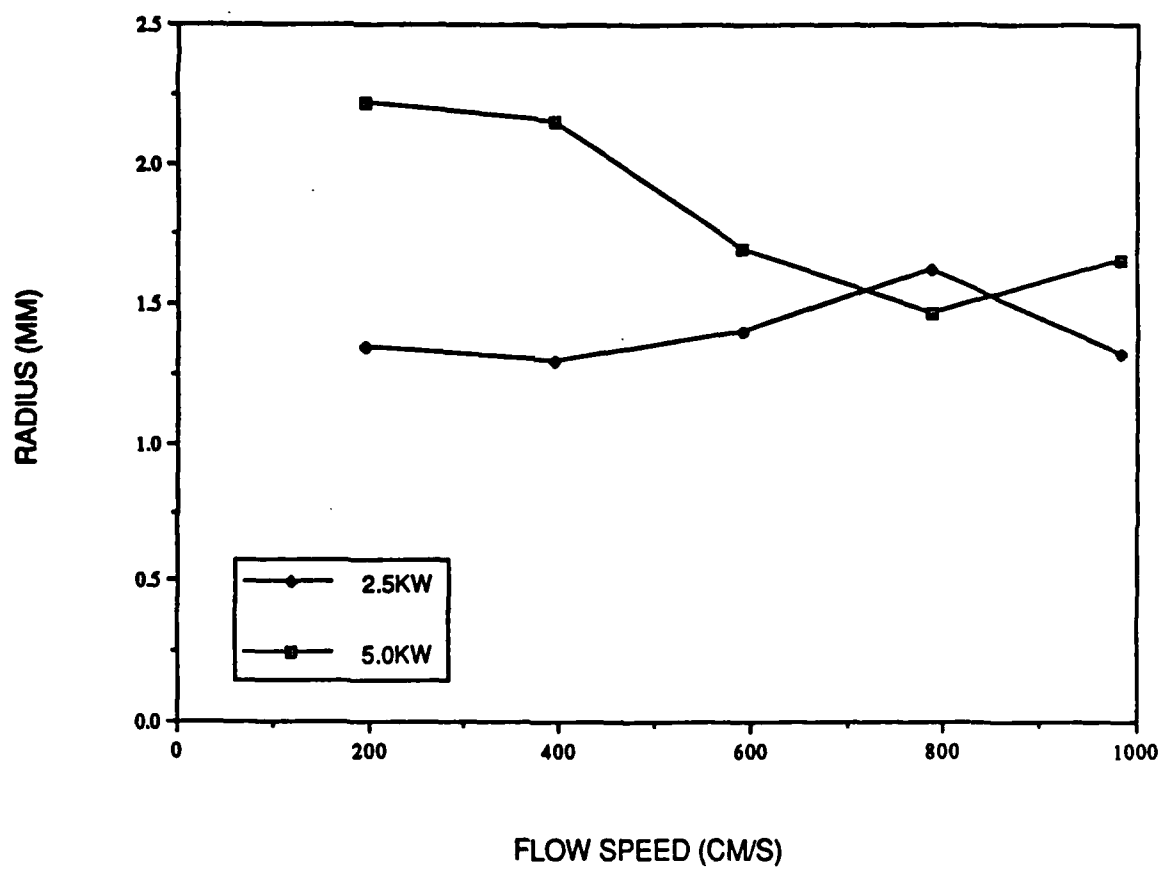


Figure 5.6 Radius of the 11,600 K temperature region versus flow speed for laser powers of 2.5 kW and 5 kW.

interact with more particles of the plasma on the path and increases the chance of the photons being absorbed. A narrower plasma also tends to reduce the radiation loss, hence elevates the thermal efficiency. The f numbers of previous experiments [20] were limited to about $f/2.4$, beside the very low flow speed (< 120 cm/sec). Here the experiments with an $f/7$ optics are reported and compared with the previous results. Errors in absorption and efficiency are within $\pm 5\%$.

5.2.1 Total Absorption

Figure 5.7 shows the total absorption versus flow speed for 2.5 kW and 5 kW laser powers. The mean flow speed is varied from 2 m/sec to 10 m/sec, with an $f/7$ optics and 1 atmosphere chamber pressure.

It is observed in Figure 5.7 that higher laser power results in higher total absorption. 58% to 75% absorption are reported for 2.5 kW, and 75% to 86% for 5 kW laser power. This is explained by the higher electron temperature in a plasma generated by higher laser power, which leads to a higher inverse bremsstrahlung absorption coefficient when temperature does not exceed 16,000 K (see Figure 2.3), which is true for the most part of the plasma as shown in Figure 5.1.

The trends of the total absorption curves versus the flow speed are similar for the two laser powers in Figure 5.7. Absorption is at its lowest at the lowest flow speed, because most of the plasma is still upstream from the laser focal point where power density is not very high. As the flow speed increases, the plasma is pushed toward the laser focus, and the absorption rises to 86% at 394 cm/sec followed by a gradual decline to 78% at 788 cm/sec. As the speed further increases, however, the absorption tends to climb again, regaining to 83% at 985 cm/sec. But the variation in absorption is not significant enough to predict a peak absorption, since the experimental error in total absorption is believed to be $\pm 5\%$. It looks very possible

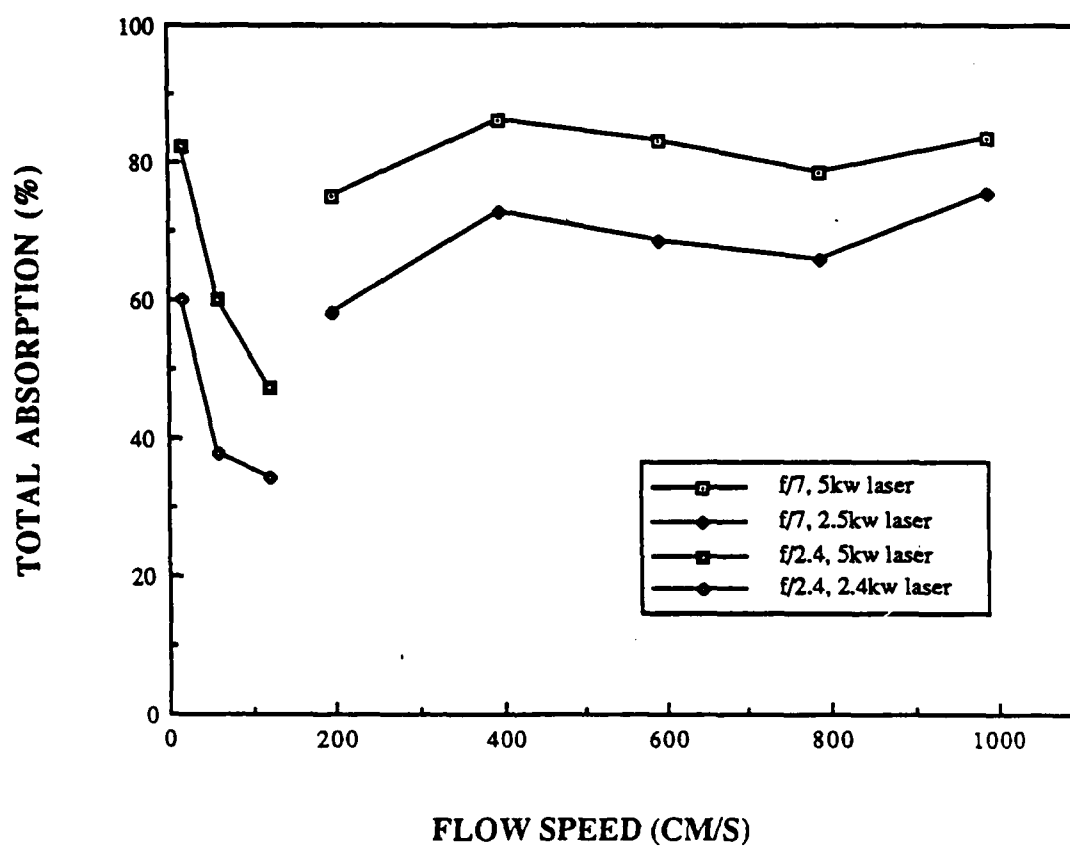


Figure 5.7 Total absorption versus argon flow speed for 2.5 kW and 5 kW laser power. 1 atmosphere chamber pressure, $f/7$ optics. The results of $f/2.4$ and low flow speed are also plotted for comparison.

that eventually the absorption will get higher, as is already the case for the 2.5 kW laser power. Further experiments with even higher flow speeds are necessary to reveal the truth.

For comparison, the results of the experiments with $f/2.4$ optics and low flow speed [20] are also plotted in Figure 5.7. The total absorption decreased as speed increased from 15 cm/sec to 120 cm/sec. Only about 40% to 60% absorption were reported for a 2.4 kW power, and 50% to 80% for a 5 kW power.

The lower absorption can be explained by three disadvantages in the old experiments. First, the smaller f number optics has a steeper focus that shortens the beam distance of travel through the plasma. Second, the convex-concave mirror pair used in the old experiments tends to have a larger focus spot size due to its off-axis optical scheme, despite its having a smaller f number. This will reduce the laser power density and result in lower electron temperature and lower absorption. And finally, there are the effects of increasing flow speed.

It is believed that the location of a plasma relative to the laser focus is an important factor for absorption. A plasma that is sustained around the focus will benefit the most from the high power density in that region. A plasma with a low flow speed will find an equilibrium position upstream from the focus. Increasing flow will push it closer to the focus. But as flow speed gets too high, the plasma will eventually pass the focal point and goes to the diverging part of the beam, which causes a decline in absorption.

Due to the steeper focus at $f/2.4$, the plasma is much easier to be pushed downstream than at $f/7$. As confirmed by the temperature plots in Reference [20], the plasma has already crossed the laser focal point at flow speed of as low as 15 cm/sec, and shifts further downstream for higher speeds. This explains why the absorption shows a simple decline for increasing flow speed in that experiment.

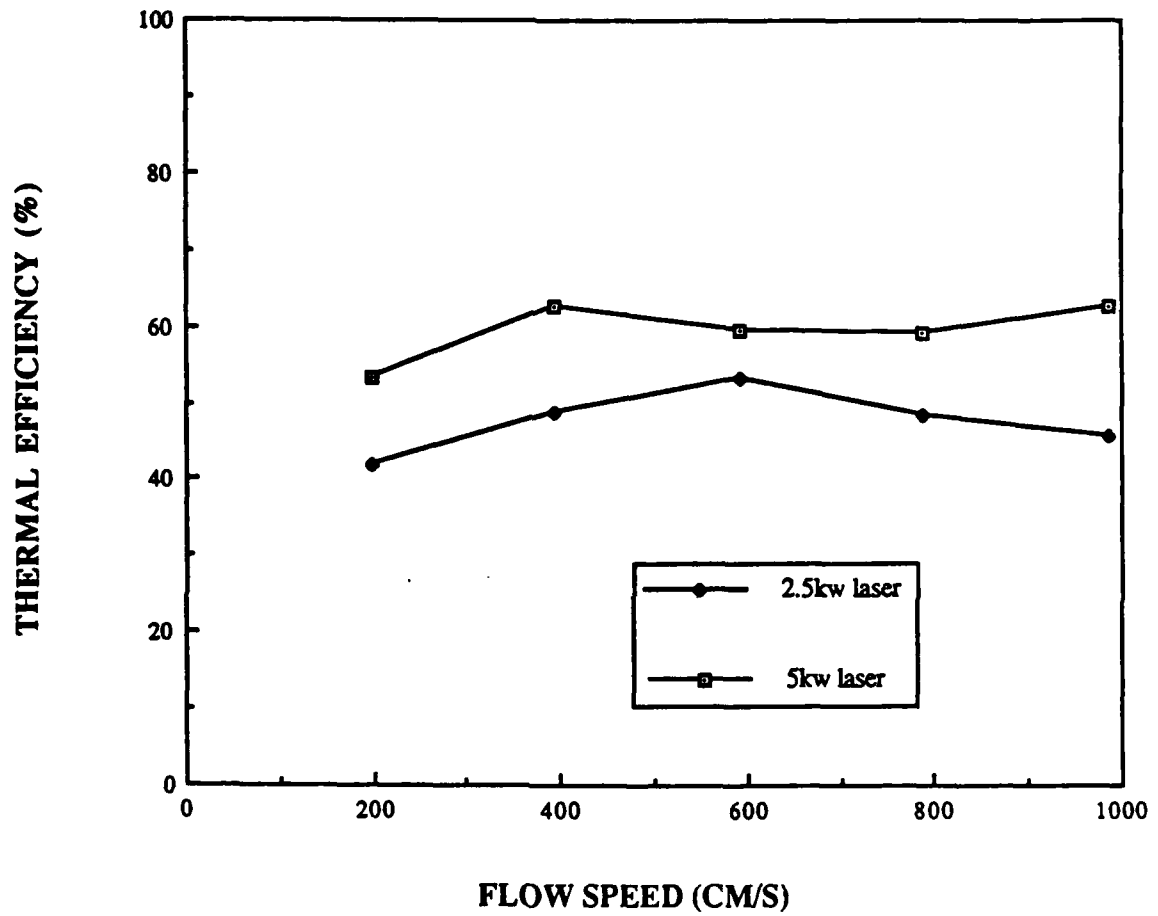


Figure 5.8 Thermal efficiency versus argon flow speed for 2.5 kW and 5 kW laser power. 1 atmosphere chamber pressure, f/7 optics.

On the contrary, the $f/7$ optics now used has higher power density upstream from the focus, thus a higher flow speed is required to relocate the plasma to the beam focal region. In fact, Figures 5.2 and 5.3 show that in our speed range of 2-10 m/sec, the plasma has not yet passed the laser focus. Thus the absorption remains high. Even higher flow speed experiments will be necessary to see any substantial decline due to the plasma position.

5.2.2 Thermal Efficiency

Thermal efficiencies of plasmas with 2.5 kW and 5 kW laser powers are presented in Figure 5.8 for flow speeds of 2 m/sec to 10 m/sec. Again the thermal efficiency is higher at higher laser power. Efficiencies between 41% and 53% are obtained for 2.5 kW laser, and 53% to 62% for the 5 kW laser. These numbers are surprisingly and encouragingly high compared to previously reported 30-40% efficiencies [20].

The concept of laser supported rocket propulsion is considered feasible if the thermal efficiency can reach at least 50%. But in a real propulsion application, the laser power will be in the order of 10-100 MW, which is much higher than the current available power level. However, the flow speed in a real rocket thruster will also be much higher than in the absorption chamber used, which will still tend to maintain the plasma in a position close to the focus. In case the laser power is still too high for the designed flow, the beam can be split into several smaller beams to support multiple plasmas, each of which has a reduced power and a maximum thermal efficiency at the flow rate.

Twin plasma experiments were performed. But due to the break of symmetry in the plasma geometry, the Abel inversion technique is no longer valid. It can not provide accurate predictions of temperature distribution.

In Figures 5.9 and 5.10, the total absorption and thermal efficiency are plotted

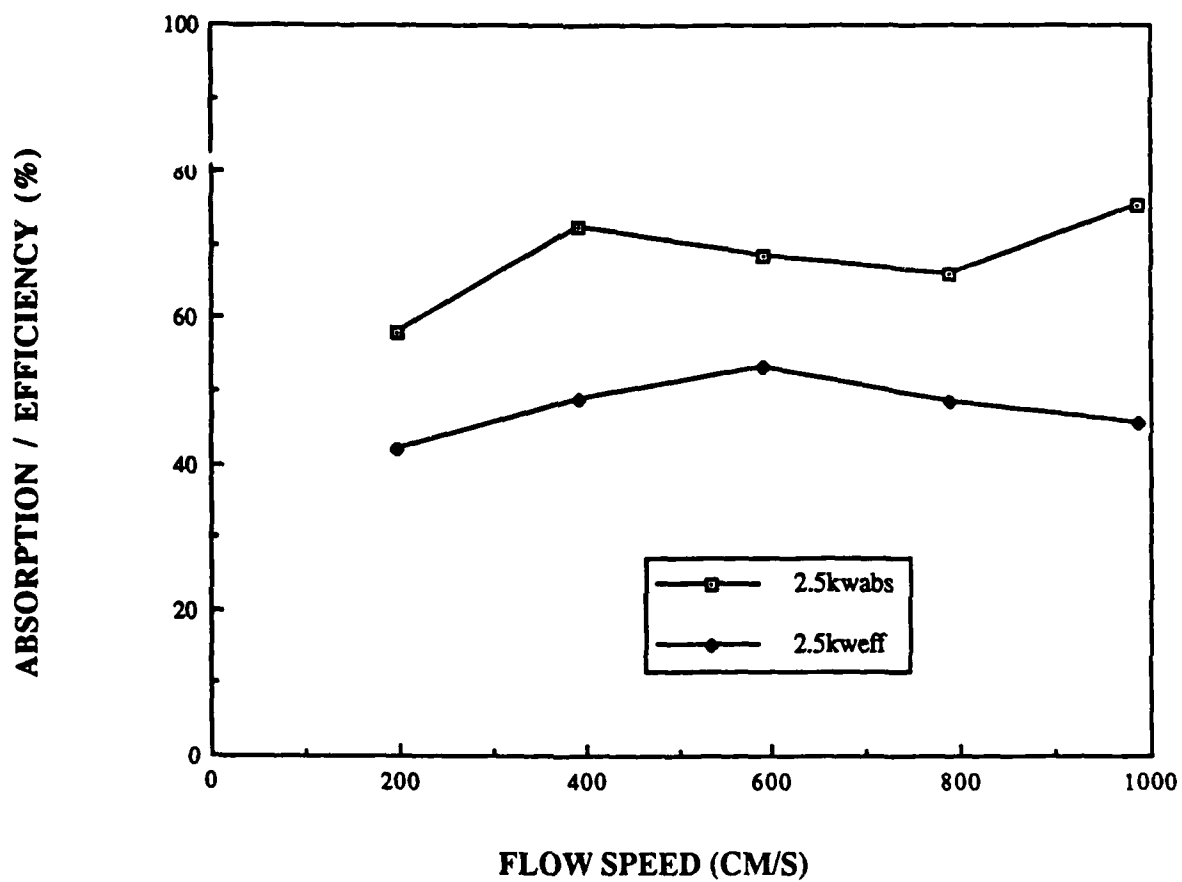


Figure 5.9 Absorption and efficiency versus flow speed. 2.5 kW laser, 1 atm pressure, $f/7$ optics.

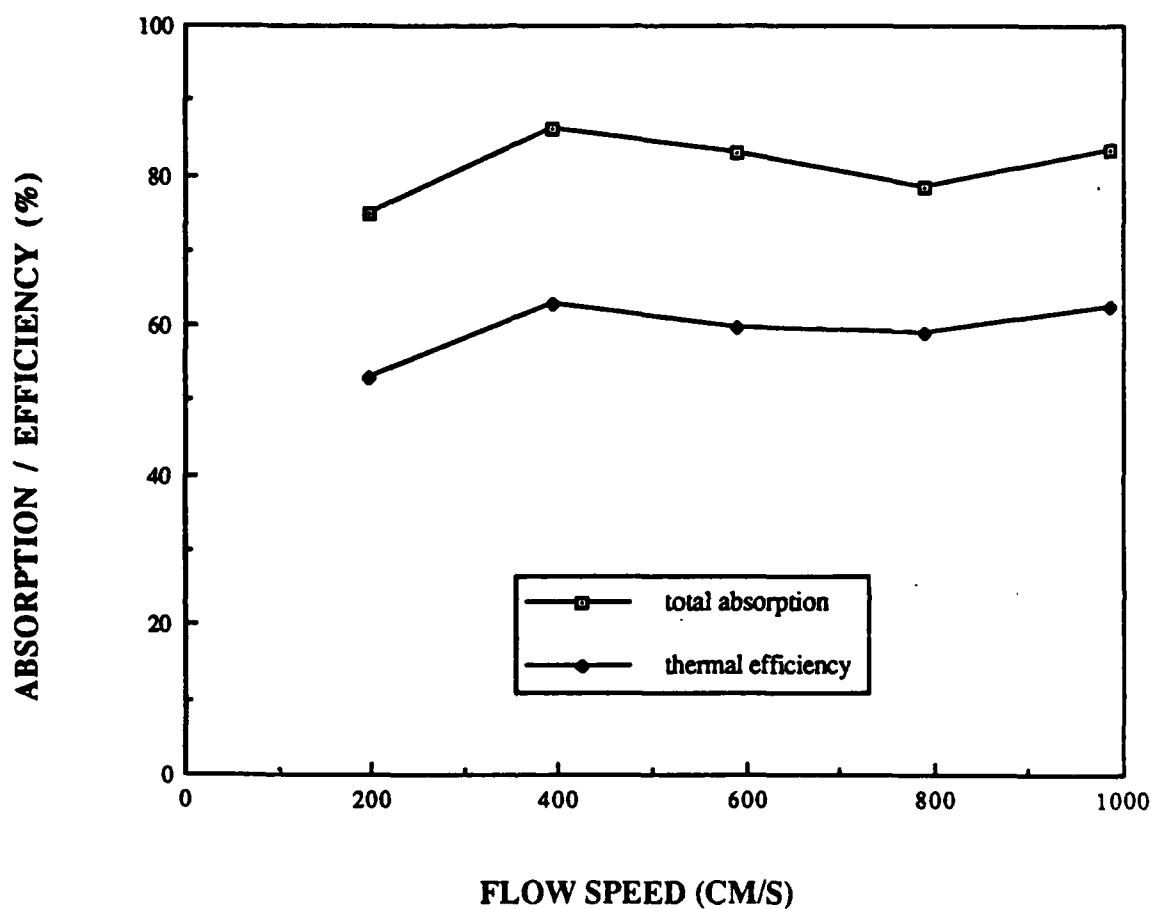


Figure 5.10 Absorption and efficiency versus flow speed. 5 kW laser, 1 atm pressure, f/7 optics.

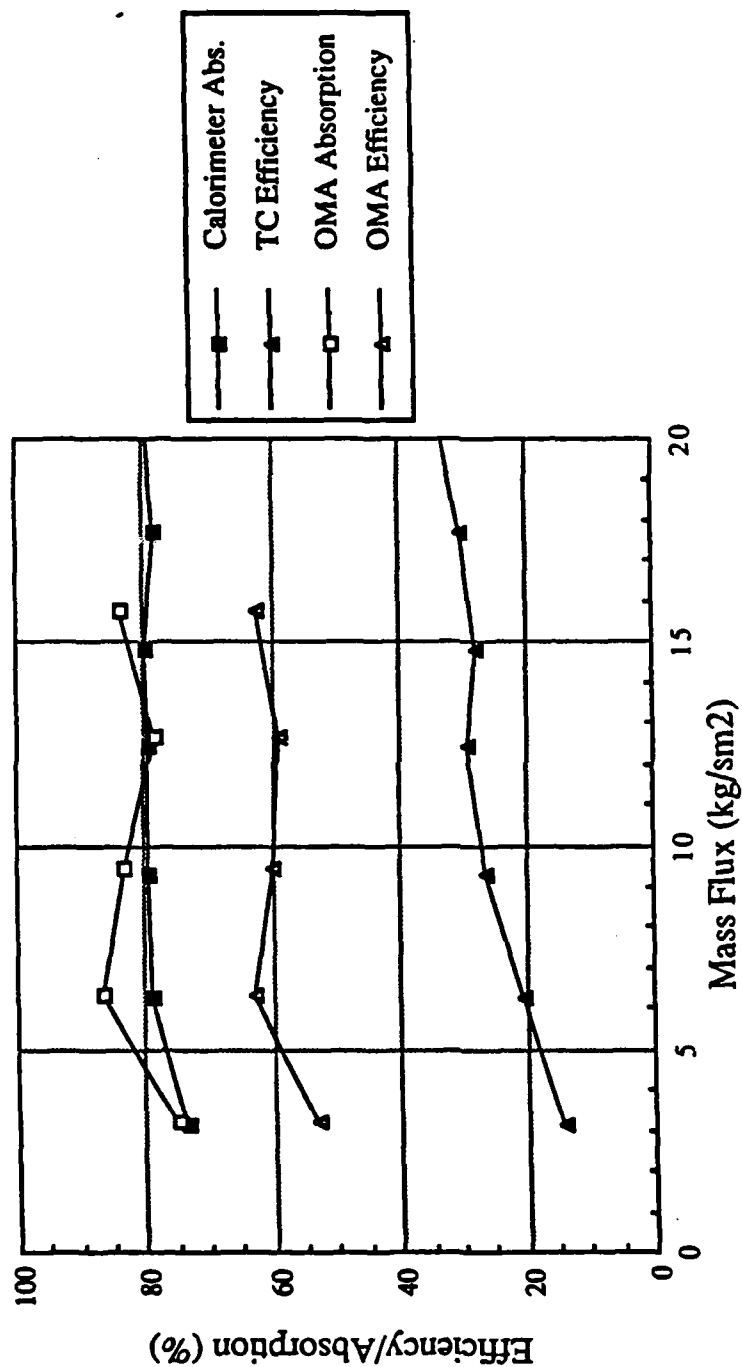


Figure 5.11 Comparison of spectroscopic results and calorimeter-thermocouple measurements for 5 kW laser, 1 atm pressure and f/7 optics.

together to show the energy transfer process. The difference between the absorption and the efficiency curves represents the fraction of the laser power that is first absorbed but then radiated by the plasma. Note that the fractional radiation is almost the same for the 5 kW laser power, which can be explained by the somewhat constant plasma volume for the 5 kW laser power described in the last section, because the radiation loss is a volume integral.

For the plasmas sustained by a 2.5 kW laser power, the fractional radiation has a little variation, which can be explained through careful examination of the plasma shape illustrated in Figures 5.5 and 5.6. Compare the first three data points, namely the length, radius, and fractional radiation at speeds of 2, 4, and 6 m/sec, it can be seen that, while the plasma radius does not vary too much, a larger plasma length results in a higher radiation loss at a flow speed of 4 m/sec. The effect of the increasing plasma length on the increase of the radiation is also obvious for the two higher flow speed data points.

5.3 Comparison with Calorimeter-Thermocouple Measurements

An independent measuring technique was also used to obtain the total absorption and thermal efficiency. The total absorption was measured by a calorimeter, and the thermal efficiency by thermocouples. Figure 5.11 shows the comparison between the results from the spectroscopic method and the calorimeter-thermocouple measurement for a plasma of 5 kW laser power.

The total absorption data from both methods agree with each other quite well, while the thermal efficiencies do not. Thermocouple method predicts efficiencies of only about 30%, compared to the near 60% obtained from the spectroscopic analysis.

At present, the big discrepancy between efficiency measurements is not well understood yet. Two major factors are cited for the possible reasons. One is the gas

heat convection loss to the chamber and duct walls as it travels from the plasma region to the exit ports where the thermocouples are positioned. This tends to underpredict the actual thermal energy retained by the gas.

The other possible reason is the too large axial increment chosen for the experiment, which was $\Delta z = 2$ mm, compared to the radial increment of $\Delta r = 0.2377$ mm. Although it means to take more time to complete a data acquisition and reduction, it is suggested to repeat experiments with smaller axial increments to examine the effect.

5.4 Recommendations

The laser sustained plasma experiment should be done for as large a range of operating condition as possible. The laser power is somewhat limited by the available CW CO₂ laser device, unless we go to pulsed laser sources such as a free electron laser. The focusing f number can be easily changed by using another lens. Changes to the gas chamber is being made to raise the chamber pressure and the flow speed. These include smaller diameter quartz tube and larger gas exit ports with valves.

Another interesting aspect is the addition of hydrogen to the currently pure argon gas. Because the real laser rocket propulsion will use light propellant such as hydrogen. The reason we chose argon to do our previous experiments is that argon has similar physical properties to hydrogen and is much safer to handle. We may first add helium to the argon flow instead of hydrogen to test the plasma stability, and gradually replace it with hydrogen.

Multiple plasmas experiment should also be pursued in order to find the optimum flow rate for very high total laser powers. Convection is expected to help preserve the gas thermal energy as cold gas passes between the plasmas. A plasma might also absorb the radiation from nearby plasmas, reducing the total radiation loss. The

difficulty in spectroscopic measurement of multiple plasmas is the break of the plasma cylindrical symmetry. Abel inversion for the multiple plasmas needs to be developed.

The current OMA method can only detect electron temperatures above 9,000 K, because the line-to-continuum ratio predicts bogus temperature when the temperature gets too low as illustrated in Figure 4.6(b). Therefore new techniques have to be developed to determine the temperatures at the outer region of the plasma and downstream from the plasma. Accurate flow velocity profiles are also necessary to describe the flow downstream. With the temperature and velocity information, accurate enthalpy change can be calculated, which will lead to better prediction of the thermal efficiency.

Laser induced fluorescence (LIF) technique seems to be the most promising solution. A Lambda Physik excimer pumped dye laser will be used to pump an atom or a molecule in the flow (seeds might be needed), which then decays and radiates a photon. The fluorescence signal can be analyzed to obtain local electron temperature [26]. Several techniques can be implemented such as one line, two line and thermally assisted LIF. Due to the very high temperatures encountered in the laser sustained plasmas, most molecular seeds will be dissociated. Atomic seeds such as gallium or indium seem to be good candidates for their high ionization potentials. One should also select seeds that will not generate too much extra free electrons to change the original plasma properties. Before trying any seeds, however, the possibility of using the flowing gas itself as fluorescence source should be fully examined.

The LIF technique has been proven effective in combustion diagnostics where temperatures are usually below 2,000 K. LIF for laser-sustained plasmas has never been attempted before.

Accurate flow velocity distribution measurement is another concern. Laser doppler velocimetry (LDV) is only good for point measurement. The method using the

Doppler shift of an LIF signal [27] has spatial resolution, but is applicable only to low pressure (a few Torr) and high velocity (greater than 30 m/sec) flows. At present, the particle image velocimetry seems to be feasible in our situation.

Appendix A: Program to Drive the Stepping Motor Controller

The motor that drives the vertical stage is specified as motor #1. The axial increment is 2 mm in the following program.

```
90    V1 = 100
100   INC = 4300
110   GET A$
120   IF A$ = "U" THEN I1=INC
130   IF A$ = "D" THEN I1=-INC
140   @:GOTO 110
RUN 90
```

Appendix B: Program to Do 2-D Temperature Contour

DI-3000 software package is used on the HP-9000 computer.

```

C
C  PROGRAM TO DO 2D TEMPERATURE PLOTTING
C
  PROGRAM PLOT2D
  DIMENSION TEMP(50,50),TEM(50,50),TE(100,100),XD(50),YD(100),
  $X(1100),Y(1100),Z(1100),ZZ(100,100),WORK(20000),IWORK(30000),
  $IARRAY(7)
  INTEGER INIPOS,ENDPOS,ENDR
C
  REAL  WLDMIN,  WLDMAX,  EYE,  AT
  DIMENSION WLDMIN(3), WLDMAX(3), EYE(3), AT(3)
C
  INTEGER LABLFG,  LABJST,  NMINOR,  ICODE
  DIMENSION      LABJST(2)
C
  REAL  AXSBEG,  AXSEND,  DELTIK,  DELLAB,  DELBAS
  DIMENSION AXSBEG(3), AXSEND(3), DELTIK(3), DELLAB(3), DELBAS(3)
C
  REAL  DELPLN,  SKPVAL,  DELLEN,  RATMIN,  DNORML(3)
  DIMENSION DELPLN(3), SKPVAL(3)
C
  CHARACTER*3 LTIT(20),CPRES,CFNUM,CPWR,CVEL
  CHARACTER*5 LINT(10),CCINT
  REAL      CINT
C
C  OPEN DATA FILES
C
  OPEN (1,FILE='tempout',STATUS='OLD')
  rewind(1)
  read(1,11) JKM,NNN,LPARM,POWER
  read(1,12) DR,DZ,Z0
11 format(3I10,5X,F10.4)
12 format(3(F10.4,5X))
  do 2 i=1,nnn
  read(1,13) (TEMP(i,k),k=1,jkm)
13 format(5(F10.4,5X))
  2 continue
  close(1)
C
  zmax=z0+float(nnn-1)*dz
  rmax=float(JKM-1)*dr
  print*,'enter initial and end axial positions to plot, in mm'
  write(6,004) z0,zmax
004 format(1X,7HZini > ,F4.0,2X,7HZend < ,F4.0)
  read(5,*) zini,zend
  print*,'wish to limit the radial dimension,too? Y=1/N=0'
  read(5,*) limrad
  if(limrad.eq.0) goto 61
  write(6,003) rmax
003 format(1X,34Henter max radial position in mm, <, 1X,F6.4)
  read(5,*) rmax
C
  endr=int(rmax/dr)+1
  goto 62
61 continue
  endr=JKM
62 continue
  print*,'preparing data matrix for plotting and stored in xyz...'
C

```

```

      inipos=int((zini-z0)/dz)+1
      endpos=int((zend-z0)/dz)+1
      nx=endpos-inipos+1
      ny=2*endr-1
      num=nx*ny
C
C   LIMIT THE REGION TO BE PLOTTED
C
      do 22 i=1,nnn
      if(i.lt.inipos.or.i.gt.endpos) goto 22
      k=i-inipos+1
      do 21 j=1,jkm
      if (j.gt.endr) goto 21
      tem(k,j)=temp(i,j)
21 continue
22 continue
C
      open (7,file='xyz')
      rewind (7)
C
C   MAP COMPLETE TEMPERATURE FIELD BY IMAGING HALF SPACE ABOUT CENTERLINE
C
      DO 300 J=1,nx
      K=endr+1
      DO 200 I=1,ny
      IF(I.LE.endr)TE(J,I)=TEM(J,K-1)
      IF(I.GT.endr)TE(J,I)=TEM(J,I-endr+1)
      K=K-1
200 CONTINUE
300 CONTINUE
C
C   GET THE INPUT DATA FOR JSSC3 AND STORE IT IN FILE XYZ
C
      Z0=Z0+(float(inipos)-1.)*DZ
      R0=-(float(endr)-1.)*DR
      DO 400 I=1,nx
      XD(I)=Z0+(float(I)-1.)*DZ
400 CONTINUE
      DO 500 J=1,ny
      YD(J)=R0+(float(J)-1.)*DR
500 CONTINUE
C
      DO 700 N=1,NUM
      DO 600 J=1,ny
      IF((N.GE.(J-1)*nx+1).AND.(N.LE.J*nx))
      $ X(N)=XD(N-(J-1)*nx)
      if((n.ge.(j-1)*nx+1).and.(n.le.j*nx))
      $ Y(N)=YD(J)
600 CONTINUE
700 CONTINUE
C
      DO 900 I=1,nx
      DO 800 J=1,ny
      N=(J-1)*nx+1
      Z(N)=TE(I,J)
800 CONTINUE
900 CONTINUE
      write(7,2001) (x(i),i=1,num)
      write(7,2001) (y(i),i=1,num)
      write(7,2001) (z(i),i=1,num)
2001 format(5(f10.4,5x))
      close (7)
      print*, 'data x,y,z are ready'
      print*, 'and stored in file xyz for inspection'
C
C   SET PLOTTING PARAMETERS

```

```

C      open(2,file='oldwork')
      open(3,file='newwork')
      open(4,file='zz')
      rewind(2)
      rewind(3)
      rewind(4)
C
      print*,'enter mode'
      print*,'      TRIANGULATION      GRIDDING'
      print*,'0:  do nothing              do nothing'
      print*,'1:  use provided data        do nothing'
      print*,'2:  use provided data        use provided data'
      print*,'3:  use provided data        perform gridding'
      print*,'4:  perform triangulation    do nothing'
      print*,'5:  perform triangulation    perform gridding'
      read(5,*) mode
      print*,'enter from,to,by (in K)'
      read(5,*) from,to,by
C
      if(mode.gt.3)goto 1000
      read(2,*)(iwork(i),i=1,15)
      jwlen=iwork(12)
      ilen=iwork(13)
      read(2,*)(iwork(i),i=16,jwlen)
      read(2,*)(iwork(i),i=1,ilen)
      niw=jwlen
      nw=ilen
      if(mode.ne.3)goto 2000
      nt=iwork(3)
      niw=iwork(9)+18*nt
      goto 2000
C
1000 continue
      nw=15*num
      niw=25*num
2000 continue
C
      Prepare iarray for max & min annotation-----
      do 31 i=1,7
      iarray(i)=-1
0031 continue
      iarray(6)=230
C
C      CALL PLOTTING ROUTINES AND STORE PARAMETERS FOR REPLOT
C
C      print*,'selet which subroutine you would like to use(use jssc3)'
C      print*,'enter 1: use jssc3'
C      print*,'      2: use tric2'
C      read(5,*) iroutine
C
      print*,'the screen will be blank for a while-- as long as 30'
      print*,'minutes or more -- please enter any number to continue'
      read(5,*) ok
C
C
      OPEN(8,FILE='setxaxs')
      REWIND(8)
      READ(8,*) (WLDMIN(I),I=1,3)
      READ(8,*) (WLDMAX(I),I=1,3)
      READ(8,*) (EYE(I),I=1,3)
      READ(8,*) (AT(I),I=1,3)
C
      call jbegin
      call jdinit(1)
      call jdevon(1)

```

```

call jssini
PRINT*, 'OI'
C  TICK MARKS ON THE WINDOW -----
C  call jssist(19,2)
C  MAX AND MIN ANNOTATION -----
call jssist(6,0)
C  call jssist(6,1)
call jssiat(10,7,iarray)
C  DISABLE CONTOUR LINE AND COLOR FILLING THE AREA BETWEEN LINES ---
C  call jssist(10,0)
call jssist(27,1)
C  SET VIEWPORT AND EYE POINT -----
CALL JWINDO(-24.,24.,-6.,6.)
CALL JSSIST(29,0)
CALL JVPOR(-0.8,0.8,-0.8,0.8)
CALL JSSPRO(WLDMIN,WLDMAX,EYE,AT)
C
call jsse3(x,y,z,num,from,to,by,zz,nx,ny,
S      iwork,niw,work,nw,mode)
C
C  PLOT AXIS WITH ANNOTATION -----
C
NAXS=1
41 CONTINUE
IF(NAXS.EQ.2) GOTO 43
IF(NAXS.EQ.3) GOTO 44
C
AXSBEG(1)=X(1)
AXSBEG(2)=Y(1)
AXSBEG(3)=10000.0
AXSEND(1)=X(NX)
AXSEND(2)=Y(NX)
AXSEND(3)=10000.0
C
READ(8,*) DELLEN
READ(8,*) NMINOR
READ(8,*) (DELTIK(I),I=1,3)
READ(8,*) RATMIN
READ(8,*) LABLFG
READ(8,*) (LABJST(I),I=1,2)
READ(8,*) (DELLAB(I),I=1,3)
READ(8,*) (DELBAS(I),I=1,3)
READ(8,*) (DELPLN(I),I=1,3)
READ(8,*) (SKPVAL(I),I=1,3)
42 CONTINUE
CALL JOPEN
CALL JSSAXS(AXSBEG,AXSEND,DELLEN,NMINOR,DELTIK,RATMIN,
&      LABLFG,LABJST,DELLAB,DELBAS,DELPLN,SKPVAL)
CALL JCI OSE
NAXS=NAXS+1
GOTO 41
C
43 CONTINUE
OPEN(9,FILE='setyaxs')
REWIND(9)
C
AXSBEG(1)=X(1)
AXSBEG(2)=Y(1)
AXSBEG(3)=10000.0
AXSEND(1)=X(1)
AXSEND(2)=Y(NUM)
AXSEND(3)=10000.0
READ(9,*) DELLEN
READ(9,*) NMINOR
READ(9,*) (DELTIK(I),I=1,3)
READ(9,*) RATMIN

```



```

      READ(9,*) LABLFG
      READ(9,*) (LABJST(I),I=1,2)
      READ(9,*) (DELLAB(I),I=1,3)
      READ(9,*) (DELBAS(I),I=1,3)
      READ(9,*) (DELPLN(I),I=1,3)
      READ(9,*) (SKPVAL(I),I=1,3)
      GOTO 42
C
44 CONTINUE
C
      if(iroutine.eq.2) goto 3000
C
      call jssc3(x,y,z,num,from,to,by,zz,nx,ny,
C
      Siwork,niw,work,nw,mode)
C
      goto 4000
C
3000 continue
      call tric2(x,y,z,num,from,to,by,
C
      Siwork,niw,work,nw,mode)
C
4000 continue
C
      Save data for replot-----
C
      write(6,00030)(iwork(i),i=1,6)
00030 format(9H IWORK = , 10I5, 3I7/8H WORK = , 6F10.3)
C
      if (mode.lt.3)goto 9000
      jwlen=iwork(12)
      ilen=iwork(13)
      write(3,*) (iwork(i),i=1,15)
      write(3,*) (iwork(i),i=16,jwlen)
      write(3,*) (iwork(i),i=1,ilen)
C
      if(mode.eq.4) goto 9000
      write(4,*) nx,ny
      write(4,*) ((zz(i,j),i=1,nx),j=1,ny)
C
9000 continue
      PRINT*, 'C'
      call jpause(1)
      PRINT*, 'K1'
      call jend
      close(2)
      close(3)
      close(4)
      close(7)
      close(8)
      close(9)
      close(10)
      stop
      end

```

References:

- [1] Kantrowitz, A., "Propulsion to Orbit by Ground-Based Lasers," *Astronautics and Aeronautics*, Vol. 10, May 1972, pp.74-76
- [2] Glumb, R.J., PhD Thesis, Department of Mechanical Engineering, University of Illinois at Urbana-Champaign, June 1986
- [3] Glumb, R.J. and Krier, H., "Concepts and Status of Laser-Supported Rocket Propulsion," *J. of Spacecraft and Rockets*, Vol. 21, January 1984, pp.70-79
- [4] Fowler, M.C. and Smith, D.C., "Ignition and Maintenance of Subsonic Plasma Waves in Air by CW CO₂ Laser Radiation," *J. of Applied Physics*, Vol. 46, January 1975, pp.138-150
- [5] VanZandt, D.M., McCay, T.D., and Eskridge, R.H., "An Experimental Study of Laser Supported Hydrogen Plasmas," AIAA Paper 84-1572, AIAA 17th Plasma Dynamics Conference, June 1984
- [6] Keefer, D., Crowder, H., and Peters, C., "Laser-Sustained Argon Plasmas in a Forced Convective Flow," AIAA Paper 85-0388, AIAA 23rd Aerospace Sciences Meeting, Reno, Nevada, January 1985
- [7] Welle, R., Keefer, D., and Peters, C., "Energy Conversion Efficiency in High-Flow Laser-Sustained Argon Plasmas," AIAA Paper 86-1077, AIAA/ASME 4th Mechanics, Plasma Dynamics and Lasers Conference, Atlanta, Georgia, May 1986
- [8] Jeng, S-M, and Keefer, D., "Influence of Laser Beam Geometry and Wavelength on Laser-Sustained Plasmas," AIAA Paper 87-1409, AIAA 19th Fluid Dynamics, Plasma Dynamics and Lasers Conference, Honolulu, Hawaii, June 1987
- [9] Carlhoff, C., Krametz, E., Schafer, J.H., Schildbach, K., Uhlenbusch, J., and Wroblewski, D., "Continuous Optical Discharges at Very High Pressure," *Physica* 103C, 1981, pp.439-447
- [10] Krier, H., Mazumder, J., Rockstroh, T.J., Bender, T.D., and Glumb, R.J., "Continuous Wave Laser Gas Heating by Sustained Plasmas in Flowing Argon," *AIAA Journal*, Vol. 24, No. 10, pp.1656-1662, October 1986
- [11] Rockstroh, T.J., and Mazumder, J., "Spectroscopic Studies of Plasma During CW Laser Materials Interaction," *J. of Applied Physics*, 61(3), pp.917-923, February 1987
- [12] Mazumder, J., Rockstroh, T.J., and Krier H., "Spectroscopic Studies of Plasma During CW Laser Gas Heating in Flowing Argon," *J. of Applied Physics*, 62(12), pp.4712-4718, December 1987
- [13] McMillin, B.K., Zerkle, D.K., Glumb, R.J., Krier, H., and Mazumder, J., "Energy Conversion in Laser Sustained Argon Plasmas for Application to Rocket Propulsion," AIAA Paper 87-1459, AIAA 19th Fluid Dynamics, Plasma Dynamics and Lasers Conference, Honolulu, Hawaii, June 1987

- [14] Mazumder, J., Krier, H., Rockstroh, T.J., McMillin, B.K., Zerkle, D.K., Chen, X., "Laser Sustained Plasmas for Application to Rocket Propulsion," Technical Report, Department of Mechanical Engineering, University of Illinois at Urbana-Champaign, UILU-ENG-87-4002, March 1987
- [15] Glumb, R.J., and Krier, H., "Two-Dimensional Model of Laser-Sustained Plasmas in Axisymmetric Flowfields," AIAA Journal, Vol. 24, No. 8, pp.1331-1336, August 1986
- [16] Kramers, H.A., "On the Theory of X-ray Absorption and of the Continuous X-ray Spectrum," Philosophy Magazine, Vol. 46, p.836, 1923
- [17] Wheeler, C.B., and Fielding, S.J., "Absorption of Infrared Radiation as a General Technique for Determination of Plasma Temperature," Plasma Physics, Vol. 12, pp.551-564, 1970
- [18] Stallcop, J.R., "Absorption Coefficients of a Hydrogen Plasma for Laser Radiation," J. of Plasma Physics, Vol. 11, pp.111-129, 1974
- [19] Dresvin, S.V. (Editor), Physics and Technology of Low-Temperature Plasmas, The Iowa State University Press, 1977
- [20] Rockstroh, T.J., PhD Thesis, Department of Mechanical Engineering, University of Illinois at Urbana-Champaign, October 1986
- [21] Horn, K.P., "Radiative Behavior of Shock Heated argon Plasma Flows," PhD Thesis, Stanford University Report SUAA-268, Stanford, California, May 1966
- [22] Kozlov, G.I., Kutznetsov, V. A., and Masyukov., V.A., "Radiative Losses by Argon Plasma and the Emissive Model of a Continuous Optical Discharge," Soviet Physics JETP, Vol. 39, September 1974
- [23] Zerkle, D.K., MS Thesis, Department of Mechanical Engineering, University of Illinois at Urbana-Champaign, May 1988
- [24] Zerkle, D.K., Schwartz, S., Mertogul, A., Chen, X., Krier, H., and Mazumder, J., "Laser-Sustained Argon Plasmas For Thermal Rocket Propulsion," AIAA Paper 88-2773, AIAA Thermophysics, Plasmadynamics, and Lasers Conference, San Antonio, Texas, June 1988
- [25] Lerner, J.M., and Thevenon, A., "Optimizing Grating-Based Systems," Lasers & Applications, January 1984 pp.89-93
- [26] Eckbreth, A.C., Laser Diagnostics for Combustion Temperature and Species, Abacus Press, 1988
- [27] Hiller, B., PhD thesis, Department of Mechanical Engineering, Stanford University, 1986